Numerical Modelling of Electrokinetic Flow in Microchannels: Streaming Potential and Electroosmosis

by

Adham Riad

A thesis submitted in partial fulfillment of the requirements for the degree of

Master of Science

Department of Mechanical Engineering

University of Alberta

Abstract

Investigating the flow-behavior in microfluidic systems has become of interest due to the need for precise control of the mass and momentum transport in microfluidic devices. In multiphase flows, precise control of the flow behavior is much more challenging as it depends on multiple parameters. The following thesis focuses on two aspects of microfluidics discussed in two chapters: the flow reversal phenomenon in streaming potential flows and the magnetic fields generated by electroosmotic and streaming potential flows. In the first chapter, the proposed microfluidic system consists of an aqueous solution between a moving plate and a stationary wall, where the moving plate represents a charged oil-water interface. A numerical model was developed to predict the streaming potential flow created due to the shear-driven motion of the charged upper wall along with its associated electric double layer (EDL) effect. Additionally, analytical expressions were derived by solving the nonlinear Poisson-Boltzmann equation along with the simplified Navier- Stokes equation in order to describe the effect of the EDL on the shear-driven flow of the aqueous electrolyte solution. Results show that the interfacial charge of the moving interface greatly impacts the velocity profile of the flow and can reverse its overall direction. The numerical results were validated by the analytical expressions, where both models predicted that flow can reverse its overall direction when the surface potential of the oil-water interface exceeds 120mV.

For the second chapter, models were constructed for the transient electrokinetics, for both the electroosmotic flow and for the shear driven streaming potential flow, in a charged nanocapillary channel. Additionally, the transient effects of ionic currents and the magnetic field generated both inside and outside the microchannel were evaluated, and the results compared with known

analytical solutions for verification purposes. In order to correctly simulate the above models, the following partial differential equations are solved together for the electrolyte continuum to capture the physics of the problem: a) the Navier-Stokes equation for the fluid flow b) Poisson-Nernst-Planck equations for the electric potential distribution and ion transport and c) Ampere-Maxwell's law for the associated magnetic field. The obtained results showed that the magnetic field detected outside of the nanochannels can be used as a secondary electromagnetic signal for biomolecules as a part of a sequencing technique.

Keywords:

Microfluidic devices; electrokinetics; electroosmosis; streaming potential; electric double layer; magnetic fields; ionic currents.

Acknowledgment

I would first like to extend my most sincere gratitude to my supervisor, Dr. Mohtada Sadrzadeh, as his support and guidance during my research have allowed me to be where I am today. I would not be in my current position if it weren't for his constant motivation.

I would like to thank Dr. Hadi Nazaripoor for our many discussions that helped me gain a deeper understanding of my work. Our discussions were invaluable and helped guide me throughout my research.

I would like to thank Dr. Behnam Khorshidi for his constant support in the writing of my thesis and papers. Your feedback was always very much appreciated.

I thank the many members of the ARWL research group at the University of Alberta. Your great company and constant support are a big part of what helped me get to where I am today.

Most importantly, I would like to thank my parents for all their love and support.

Table of Contents

List of Figures

List of Tables

Nomenclature

ϵ	Solvent permittivity
ξ	zeta potential
κH	Dimensionless channel gap
z_i	Ion valence
D	Ion diffusivity
T	Temperature
μ	Fluid viscosity
e	Magnitude of the electron charge
K_B	Boltzmann constant
μ_0	Vacuum permeability
μ_r	Relative permeability of air
J	Current Density
t	Time
p	Pressure
$\mathbf{u}$	Velocity vector
ρ	Fluid density
n_p, n_n	Ion concentration for positive and negative ions
n_∞	Ion concentration in bulk
ρ_f	Free charge density
ψ	Electric double layer potential
Φ	Total electric potential
E_x	Applied electric field
$\mathbf{B}$	Magnetic flux density vector
$\mathbf{H}$	Magnetic field strength vector
a	Nano-capillary radius
σ_∞	Fluid conductivity

$\boldsymbol{H}$	Microchannel height
$\boldsymbol{M}$	Molar mass
$\boldsymbol{\rho}$	Density
$\boldsymbol{N_A}$	Avogadro's number
$\boldsymbol{Kn}$	Knudsen number
$\boldsymbol{\lambda}$	Mean free path
$\boldsymbol{L}$	Microchannel length
$\boldsymbol{V_{eof}}$	Electroosmotic slip velocity
$\boldsymbol{\eta_{eof}}$	Electroosmotic mobility
$\boldsymbol{k_b}$	Conductivity
$\boldsymbol{\Delta U}$	Streaming potential
$\boldsymbol{\Delta p}$	Pressure difference
$\boldsymbol{\kappa, \lambda_d}$	Debye length

1 Introduction

1.1 Microfluidic devices

The lab-on-chip devices are a promising field of technology operational on the micro- and nanoscales, advancing applications in the biomedical and chemical sectors [1,2]. They are microdevices that create laboratory techniques on a single chip that is no bigger than a few square centimeters in size [1,2], allowing for the integration of entire biological and chemical experiments and tests on the single chip [3]. Their fabrication became possible after the booming of silicon microfabrication devices in the 1980s, which gave room to the development of the lab-on-chip devices [4]. The development of the lab-on-chip devices is expected to have a revolutionary effect in the chemical and biological fields as circuits had in the electronics field [3]. The size of these lab-on-chip devices allows for the manipulation of microscale reagents such as those found in DNA analysis, cell sorting, automation, among other techniques [5]. The lab-on-chip devices allow for both single-unit operations, such as droplet generation, mixing, separation, detection and heating or a combination of multiple operations that are integrated together [4]. These lab on chip devices are able to do those laboratory techniques due to their integration of both active and passive components with microfluidic channels [3]. Because of their size, lab-on-chip devices allow for minimally invasive procedures because they require only a very limited number of samples to run their tests, making them environmentally friendly as well. However, due to the degree of precise system integration that goes into them, they need continual technological developments to ensure the optimum results [3].

The fundamental notion of lab-on-chip devices is based on the science and engineering of fluid flow in microscale ranges, known as microfluidics [1]. Microfluidics is the science and technology

of manipulating microchannels with at least one dimension that is one mm or less [4,6], with small amounts of fluids ranging between $10^{-9} - 10^{-18}$ L [6]. It is a platform that has profoundly been shaping the interdisciplinary fields of chemical and biological sciences, including chemical analysis, separation, and detection techniques [4,7]. This was all enabled by the very small volumes of samples and reagents that are needed in microfluidic devices, such as the lab-on-chip devices [4]. Fundamentally, microfluidics is a subdiscipline of fluid dynamics as the underlying equations that describe the physics of the fluid motion in fluid dynamics at larger scales are identical to those of microfluidics [8]. However, the main obvious difference between fluid dynamics and microfluidics is the much smaller size of the microchannels in microfluidic systems, which makes the physics of fluids much more different [8]. For example, fluid flow in macrochannels is predominantly turbulent; however, they are mainly laminar in microchannels. In addition, other phenomena such as surface tension become more significant in microchannels due to the negligible effects of gravitational forces. Since the effects of turbulence and gravitational forces are not considered in microfluidics, the physics of fluids becomes a simplified version of the more complex non-linear inertial physics associated with general fluid flow [8]. However, other forces play a substantial role in microfluidics which makes studying physics a lot more challenging. In particular, electrostatic interactions and diffusion of ionic species are two aspects that make the intrinsic characteristics and nature of fluid flow in microscale different than that in macroscale.

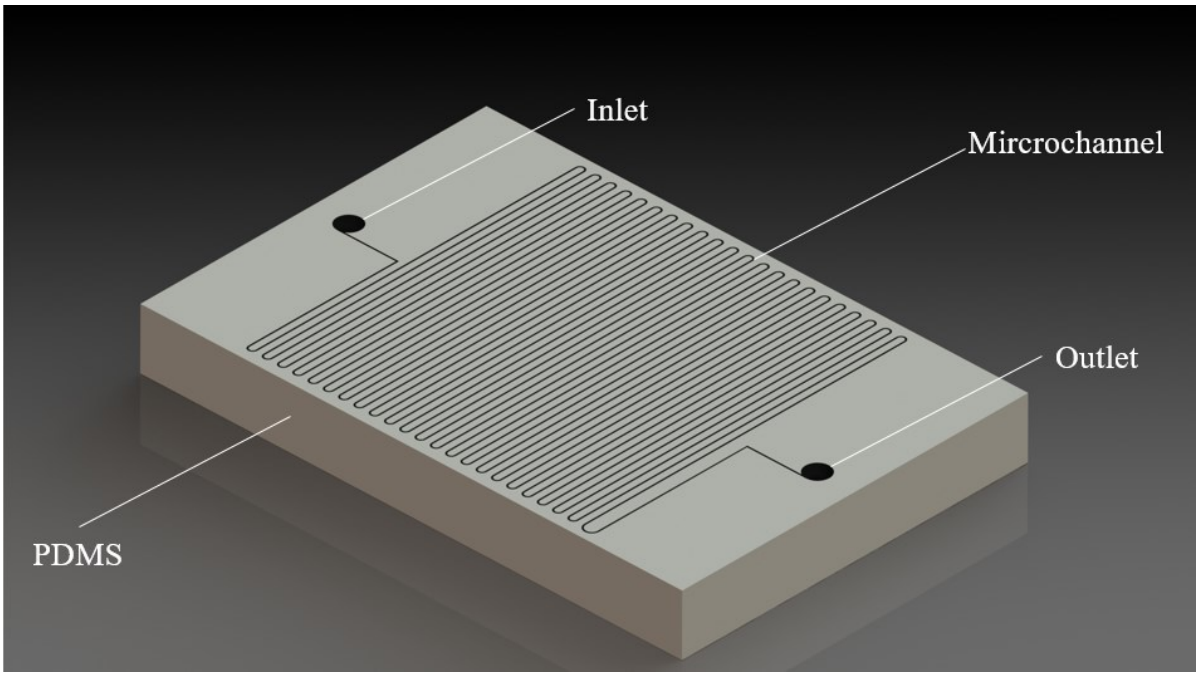

Figure 1.1 Schematic of a typical microfluidic chip

1.1.1 **Is the continuum approach valid for microfluidics?**

The momentum and continuity equations are typically used to describe macroscopic flows where the fluid is treated as a continuum. Similarly, microfluidic flows can also be described using the continuum approach. However, one needs to calculate Knudsen number, Kn, which is a nondimensional parameter that compares the mean free path of the fluid molecules to the characteristic length of the problem. This is done to ensure the validity of the continuum assumption. The continuum assumption is only valid for flows with Knudsen number lower than 0.1.

$$Kn = \frac{\lambda}{L} \tag{1.1}$$

$$\lambda = \left(\frac{M}{\rho N_A}\right)^{\frac{1}{3}} \tag{1.2}$$

Where λ is the mean free path, L is the characteristic length of the flow, ρ is the density, M is the molar mass and N_A is Avogadro's number. λ is typically assumed to be identical to the intermolecular distance for fluids. For water, the average intermolecular distance is around $0.3nm$[9]. In this study, the continuum assumption is applicable as Kn is comparably smaller than 0.1; $kn \sim 3\ x\ 10^{-4}$.

1.2 Electric double layer

In microfluidic devices, the main phenomenon that is crucial for electrokinetic transport and revolves around particles in the electrolyte is known as the electric double layer. This layer has a central role in the electrostatic stability of colloidal particles. When positively charged ions are adsorbed on the surface of a colloidal particle, the surface of the particle becomes positively charged. The now positively charged particle will attract surrounding negative counterions. The layers of charge surrounding the particle are what make up the electric double layer, which has an overall neutral electric charge [10,11]. The formation of this layer is due to the microchannel's ability to acquire polarity when putting into contact with an electrolyte [11]. The electric double layer can be divided into two regions with different charges: the stern layer and the diffuse layer. The stern layer consists of immobile counterions that attach themselves to the charged surface of the microchannel; they have an opposite charge to the surface charge [11,12]. The diffuse layer, on the other hand, contains free mobile ions that have a lower concentration as compared to the stern layer's counterions concentration, Figure 1.2 [10].

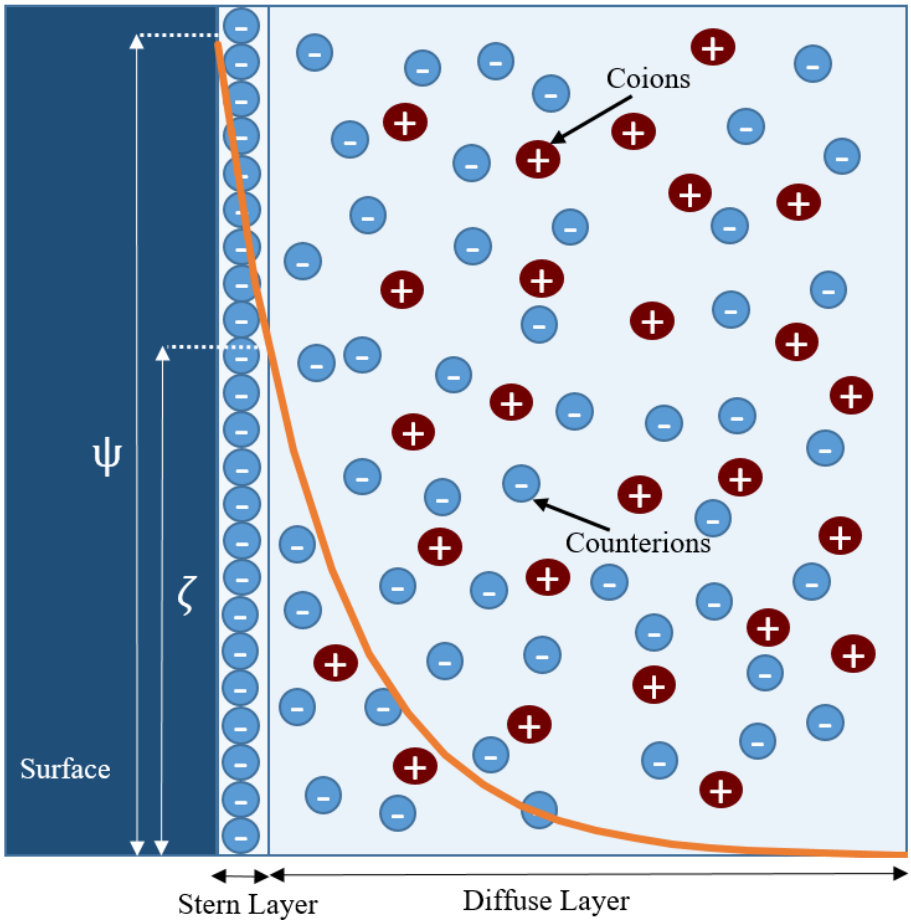

Figure 1.2 Electric double layer showing both the stern layer and the diffuse layer.

When the diffuse layer begins experiencing an electrical potential gradient, the layer of mobile ions begins to move, carrying the electrolyte with it. The applications of this process are abundant in dewatering techniques, wastewater management and the treatment of colloidal suspensions [11]. Together, the thickness of the stern layer and the diffuse layer, known as the electric double layer, is described by the Debye-Huckel equation. The characteristic length of the electric double layer is referred to as the Debye-layer thickness, λ_d, and is described using the following equation [13]:

$$\lambda_d = \left(\frac{\epsilon K_B T}{2e^2 z^2 n_\infty}\right)^{1/2} \quad (1.3)$$

Where K_B is the Boltzmann constant, n_∞ is the bulk ionic concentration, ϵ is the electrical permittivity of the medium, e is the electron charge, z is the valency and T is the temperature. It is important to note that the Debye length is a characteristic of the electrolyte solution, and gives information about the valence and bulk concentration of the ions and dielectric permittivity of the solvent.

1.2.1 **Zeta potential**

Another important characteristic of the electric double layer is the zeta potential. When a colloidal particle flows in an electrolyte, some of the electrolytic solutions adhere to the surface of the particle. The boundary that forms within the electric double layer between the particle and the electrolyte is referred to as the shear plane, or the slipping plane, where the velocity of the liquid is zero [10,14]. The value of the electric potential in the electrolyte at the shear plane, which is located between the stern layer and the diffuse layer, is defined as the zeta potential [10,15]; the streaming potential phenomenon is a good method for measuring the value of the zeta potential [16]. The zeta potential, ζ, is a function of the streaming potential, U, pressure difference between the sides of the microchannel, p, the relative permittivity of the liquid, ε, the permittivity of vacuum, ε_0, the viscosity of the fluid, μ, and the conductivity of the electrolyte, k_b [16].

$$\zeta = \frac{\Delta U}{\Delta p} \frac{\mu}{\varepsilon \varepsilon_0} k_b \quad (1.4)$$

Understanding the properties of the zeta potential makes it a great tool for numerous fields, including fluid dynamics, such as colloid stability, the flow of colloidal suspensions and measuring the charge of membranes' surfaces [10,14]. For example, the stability of colloid suspensions can

be determined by the zeta potential; this is done by understanding the interactions between the fluid particles [14]. Moreover, the polarity of the zeta potential can change from positive to negative as the pH level of the electrolyte increases; this attribute can influence fouling in membranes, where charged particles are accumulated on the surface of the membrane [16]. Additionally, it is an essential factor in determining the velocity of an electrolyte in microfluidic applications. When modeling applications of microfluidics and running simulations, zeta potential values become important factors for setting boundary conditions [14].

1.3 Electrokinetic phenomena in microfluidic devices

The renewed interest in electrokinetic transport phenomena principally stems from the necessity of moving fluids in extremely narrow confinements or channels. The capability of driving fluids through macroscopic channels, using pumps, for instance, is inapplicable in microchannels where there needs to be a great pressure difference for fluids to be transferred through capillaries on the microscopic scale. For this reason, great efforts have been put into trying to find alternative methods of transferring fluids through microchannels without the necessity for such high pressures; electrokinetic transport phenomena was selected as the most viable solution for this problem [12]. Electrokinetic flow refers to the flow of an electrolyte moving in narrow channels between two charged surfaces, driven by the combined effects of electric fields and fluid flow pressures [7,17]. The phenomena of electrokinetic transport occur when the free layer of ions in the electric double layer, explained later in this section, is sheared off. Following this, the charged ions in the free layer consequently move in a certain direction, carrying the solvent along with them. An electric field is usually induced when there is motion between the charged surfaces and the electrolyte. There are numerous phenomena that can take place when there is relative motion

between the charged surfaces and the electrolyte; the following thesis will only focus on electroosmosis and streaming potential [12].

1.3.1 **Electroosmosis**

Electroosmosis occurs when the electrolyte bulk solution is carried against the charged surface due to an external source of an electric field [18,19]. An electroosmotic pressure is a pressure needed to counterbalance the electroosmotic flow [12,20]. If the capillary wall is negatively charged, then there will be an excess of positive ions in the electrolyte. Due to the applied electric field, the positive ions in the electrolyte will begin moving towards the cathode, drawing the electrolyte along with them and resulting in a fluid flow in that direction [12,21]. The magnitude of the resulting fluid velocity depends on a parameter called electroosmotic mobility which is described by the following equation [21].

$$\eta_{eof} = \frac{\epsilon_e \zeta}{4\pi\mu} \tag{1.5}$$

Where η_{eof} is the electroosmotic mobility, ϵ_e is the electrical permittivity of the fluid, ζ is the zeta potential of the capillary walls, and μ is the fluid viscosity. If the electroosmotic mobility is large enough, it can drag all the different species within the electrolyte downstream, regardless of the polarity of their surface charge [21]. Helmholtz-Smoluchowski utilized electroosmotic mobility to explain the electroosmotic flow phenomenon. His theory proposed that the applied electric field acts on free mobile ions in the diffuse part of the double layer, explained later in this section, which drags the fluid to produce an effective slip velocity outside the double layer, given by the following Helmholtz-Smoluchowski equation [22].

$$V_{eof} = \eta_{eof} E \tag{1.6}$$

Where V_{eof} is the electroosmotic slip velocity and E is the applied electric field strength.

1.3.2 **Streaming potential**

Streaming potential flow is an electrokinetic phenomenon that arises due to the relative motion of the fluid with respect to a charged wall in a microfluidic channel. Net charges near the charged wall are carried by the fluid giving rise to a convective current in the downstream direction called streaming current.

The streaming potential phenomenon is considered as the reciprocal process of the electroosmosis phenomena [12,16,23]. When an electrolyte is forced to move through a stationary charged capillary, either by relative motion between the electrolyte and the charged wall surface or a difference in reservoir pressures from opposite ends of the capillary, an electrical potential difference is formed between the ends of the capillary [12,23]. This electric potential is often referred to as the streaming potential. The counter-ions, ions in the electrolyte that are opposite to the charged surface, are carried away with the motion of the electrolytic fluid. This motion causes the charges to accumulate at the ends of the capillary and induce a streaming potential and, in turn, an electric field. The motion of ions, due to the fluid flow, gives rise to a convective current often referred to as the streaming current [12,23]. Movement of an electrolyte in thin microchannels, driven by a pressure gradient, is considered as one of the most common ways of moving fluids in porous media and microchannels [7]. The streaming potential flow is the underlying concept of membrane-based separation of electrolytes. The streaming potential flow leads to the rejection of the ions in the microchannel and creates a different gradient of ions between the two ends of the capillary, thus allowing for the membrane-based separation [7]. A common application of the streaming potential phenomena is in seawater desalination [12].

1.4 Magnetic fields

There is ample literature discussing the flow dynamics of an electrolyte in microchannels, both in electroosmotic flow and streaming potential flow. However, not much literature is found on the magnetic fields that are induced by the electrokinetic flows in the said microchannels. The magnetic fields in the charged microchannels are induced by both time-varying electric fields and ionic currents, even though the ionic currents do not have a definite linear path to flow in (e.g. wire) [24]. The governing equations for the induced magnetic fields are the Poisson-Nernst-Planck equations, responsible for the transport of ions by convection, diffusion and migration, Naiver-Stokes equations, responsible for the flow dynamics of the electrolyte, and Ampere-Maxwell law, responsible for the induced magnetic fields. In Chapter 3, the magnetic field along with the ionic currents generated due to electrokinetic flows will be discussed with the aid of numerical models.

1.5 Literature review

The above concepts are all very important building blocks for the two chapters introduced in this thesis. Those building blocks have been studied in relation to one another in previous works.

Sheffer et al. [25]worked on three-dimensional modeling of streaming potential for single-phase flows. They were able to develop a 3D finite volume algorithm for calculating the streaming potential distribution resulting from fluid flow in a porous medium. This satisfied the need for 3D modeling capability to precisely capture the flow regime in problems of complex geometry. However, their work focused on the pressure-induced streaming potential and did not discuss multilayer oil-water systems. Sherwood et al. [26] looked at the streaming potential developed by a bubble passing through a capillary. They were able to develop a numerical model that can predict the streaming potential generated first by a single charged particle in a charged capillary, and then

by a line of particles in the same capillary. However, they concluded that their model cannot be used to analyze streaming potentials due to flow adjacent to oil-wet surfaces.

Kuang et al. reported a thorough assessment of the transient effects of electroosmotic flow in a microcapillary [27]. Yang et al. presented the transient effects of electroosmotic flow within slit microchannels [28]. They derived the analytical solutions for fully developed laminar electrokinetic flow of liquids subjected to an applied voltage. Likewise, Rice et al. researched the analytical solution for the current distribution that occurs in microcapillaries for different channels and electrical double layer lengths [29]. The analytical studies that have been conducted around the steady-state effects that occur inside electroosmotic flow driven devices, due to current and magnetic fields, have been a great aid for advancements in applications using solid-state charged nanopores, such as DNA sequencing, biomedical analyses and genetics' research [30–34]. The magnetic fields and ionic currents, induced by the applied electric potentials and generated from the flow of single charged biomolecules, such as DNA, RNA and proteins, can be used to produce a unique electronic signal. The generated electronic signals can be used for direct label-free sequencing of biomolecules. Nevertheless, current research is still being conducted on how to reduce the translocation velocity in order to allow for more accurate sensing of DNA molecules [35,36].

Together, both the first and second chapters aim to address topics that were not thoroughly studied in the literature. Some of the pertaining issues with literature in electrokinetic flow are the predominant assumptions of steady-state flow during transport and microchannels having infinite lengths. Such assumptions do not allow the understanding of the effect of charges present at the inlet and exit of the microchannel. Moreover, the assumption of an infinite microchannel enables the assumption of only a radial change in ion concentration, using the one-dimensional Poisson-

Boltzmann equation, and ignores the variation of ion concentration in the axial direction, which can be studied using the extended Nernst-Planck equations. Both the first and second chapters ensure an accurate analysis of flow in microchannels with suitable boundary conditions and assumptions. This is done to study the flow reversal in shear driven streaming potentials (first chapter) and the induced magnetic fields in electroosmotic flows and shear-driven flows (second chapter). The first chapter focuses on Flow Reversal in a Shear Driven Charged Slit Microchannel. As previously mentioned, streaming potential occurs when there is a pressure gradient in the electrolyte between the inlet and exit of the microchannel, leading to a flow of the electrolyte against the stationary charged surface [12,23]. This chapter studies the concept of a shear driven slit, where both the electrolyte and charged surface are moving, mimicking the motion between an oil-water interface. Over the years, many researchers have studied the effect of streaming potential in single-layer flows and multi-layer flows, but the analysis never fully enveloped a 3D model for multi-layer flow in an oil-water microchannel system [25,26,37,38].

The formation of an electric double layer in a fluid-liquid interface is similar to that of a solid-liquid interface. In a fluid-liquid interface, the electric double layer is formed on the water interface because of the ions present in the water [39,40]. However, the difference between a fluid-liquid interface and a solid-liquid interface is the mobility of the fluid-liquid system, representing a moving charged surface [41]. In a solid-liquid interface, the solid is immobile, representing a stationary charged surface. In addition to studying the fluid-liquid interface with a shear driven multi-layer flow, this chapter focuses on 3D modeling a slit microchannel with a finite length and includes a transient analysis. Pertinent assumptions in the literature include the analysis of steady-state flows in microchannels with infinite lengths [7]. Such assumptions are used to simplify the more complex interactions of an oil-water system, and so fail to accurately model the exact flow

in the multi-layer systems that have known inlet and exit conditions and transient flows. The second chapter of this thesis proposes a numerical model to evaluate the transient effects of internal and external magnetic field strengths for both the electroosmotic flows and shear driven streaming potential flows in charged nanochannels. Literature has previously proposed numerical models to evaluate the internal and external magnetic fields in pressure-driven streaming potential flows, but with little or no information about the transient effects of current distributions and their effect on the generated magnetic fields [24]. Another main objective of the second chapter is to evaluate the transient effects of ionic currents and the magnetic field generated both inside and outside the microchannel and verify the obtained results by comparing them with known analytical solutions.

1.6 Thesis objectives

The thesis objectives can be divided into two parts. The first part deals with analyzing the flow field of multilayered streaming potential flows while the second part is concerned with the ionic current and magnetic field generated due to electrokinetic flows.

The specific goals of the first section are to:

a) Understand the shear driven streaming potential flow in multilayer flows, i.e. oil-water interface;
b) Model the flow reversal phenomena that takes place in shear driven streaming potential flows, while incorporating inlet and exit boundary conditions and transient fluid flows in the system.

The specific goals of the second section are to:

a) Construct a model for transient electrokinetics for electroosmotic flows in a charged nanocapillary channel using a described system of equations explained more in-depth within the chapter;
b) Construct a model for the transient electrokinetic effects inside a charged nanoslit channel for a shear driven streaming potential flow inside a slit microchannel using the same system of equations;
c) Evaluate the transient effects of ionic currents and the magnetic field generated both inside and outside the microchannel and compare these results with known analytical solutions for verification purposes.

1.7 Overview of the thesis

The thesis is divided into two chapters in a paper-based format. The general idea of this thesis is to model different types of electrokinetic flows for different geometries of microchannels. In Chapter 2, a time-dependent numerical model governed by the Navier-Stokes and Poisson-Nernst-Planck equations was developed for a shear-driven slit microchannel. The model addresses the transient behavior of multilayer flows, i.e. oil-water in a finite length slit microchannel. The model also predicts the flow reversal phenomenon that occurs in streaming potential flows. In Chapter 3, the model was then extended to include the transient effects of the magnetic field and net ionic current induced due to electrokinetic flows. An electrical analogy was made to analyze the magnetic field distribution both inside and outside of the microchannel. Finally, in Chapter 4, a summary of the work done as well as directions for future work are presented.

Chapter 1

2 Flow Reversal in a Shear Driven Charged Slit Microchannel

2.1 Introduction

The popularity of lab-on-chip devices has been advancing in recent years as they are becoming of importance to biomedical applications such as clinical testing, DNA analysis [42–44] and electrophoretic separation [45]. Understanding the flow behavior in microchannels of the lab-on-chip devices is fundamental to the development of accurate and reliable measuring instruments. Precise control of the mass and momentum transport in microfluidic devices has allowed for faster analysis and processing times. These improvements enabled lab-on-chip devices to profoundly transform chemical analysis, separation and detection techniques in various applications.

Common techniques for sample separation and detection are stream potential flows and electrophoresis. The capacity of electrophoresis in clinical analysis was studied by Shang et al., where they concluded that it was one of the leading developments in separation science [46]. The injection and separation of biosamples, such as proteins and DNA, is an example of a separation technique utilized in lab-on-chip devices, where electrokinetics play an important role.

Stream potential flow is an electrokinetic phenomenon that arises due to the relative motion of the fluid with respect to a charged wall in a microfluidic channel. Net charges near the wall are carried by the fluid giving rise to a convective current in the downstream direction called streaming current. These charges accumulate downstream setting up an electrical potential, which causes an electrostatic force to act on the charges in the fluid and impact the flow dynamics and regime. This trans-capillary potential, created by the imbalance of charges near the entrance and exit, generates a conduction current in the direction opposite to the streaming current that travels through any electrical path available. At a steady state, the conduction current cancels out the convective ionic flux; the transcapillary potential generated at the ends of the channel is called streaming potential.

The streaming potential phenomenon has been observed several decades ago where the fluid flow coupling with electrical potential is often referred to as electrokinetic coupling [47]. Over the years, many researchers have studied the streaming potential for single-phase flows in microchannels. Titov et al. investigated the streaming potential and polarization effects that take place in porous media and oil pumping [37,38]. Sheffer et al. worked on three-dimensional modeling of streaming potential for single-phase flows [25]. As for multiphase flows, Sherwood et al. looked at the streaming potential developed by a bubble passing through a capillary [26]. However, no light was shed on the impact that streaming potential has on the flow distribution.

Electroosmotic and electrophoretic transport for a single-phase flow has been extensively investigated both theoretically [48][12] and experimentally [49–51]. However, numerous microfluidic devices rely on electroosmotic and electrophoretic transport of multiphase flows despite their more complex nature. Ding et al. investigated the use of multiphase flows in nanofluidic channels for electrokinetic energy conversion [52]. Ding et al. proposed using the streaming potential induced by two immiscible fluids to harvest energy, and suggested a theoretical model to measure the performance of their device. However, the model primarily focused on calculating the efficiency of energy extraction and did not explore other aspects associated with the multiphase flow within the device, such as the development of the streaming potential and the electrokinetic flow profile. To the extent of our knowledge, no model addressing these issues has been found in the literature.

In order to understand the effect of streaming potential on multiphase flows, one must first look at the reason behind the existence of electrokinetics in two-phase flows. It is renowned that the electrostatic charges on a solid-liquid interface are the reason behind the formation of an electric double layer (EDL) [53]. Similarly, the liquid-fluid interface can also be electrically charged due

to the presence of the dissolved ions or colloidal particles [39,40]. For an oil-water interface, the EDL is formed on the water side of the interface since only the water has ions. However, the only major difference between solid surfaces and liquid fluid interfaces is the fact that fluid-liquid interfaces are mobile and thus act similar to a moving charged surface. For example, if a DC electric field is applied to the oil-water system, an electrophoretic force will be exerted on the mobile interface dragging the charges and causing the entire interface to move. This mobile charge interface phenomenon has been studied by Wang et al. recently for the case of an oil bubble in water [41]. However, no model was proposed to explain the effect of streaming potential on the multiphase flow of the oil bubble in water. The following paper will propose a model for multiphase flows in a slit microchannel. The proposed system consists of an aqueous solution between a moving plate and a stationary wall, where the moving plate represents the charged oil-water interface. The model will be mainly used to study the development of streaming potential and the electrokinetic impact of the moving interface has on the velocity profile.

2.2 Problem statement

2.2.1 **Geometry**

A simplified geometry of the microchannel was used to analyze the flow behavior analytically, where the upper charged wall (i.e. the oil-water interface) represents a moving wall with a velocity of U, as shown in Figure 2.1 (a). Figure 2.1 (b) shows a more realistic geometry that was implemented in our numerical model. The geometry consists of two reservoirs, where the bulk conditions of the aqueous solution dominate, connected by a slit microchannel of length L and height H. The slit microchannel has an aqueous electrolyte solution flowing within it, sandwiched between a stationary electroneutral plane and a moving charged wall. The microchannel moving

wall is treated as a dielectric material having a surface charge that corresponds to a surface potential; this is explained using the following relation: $-0.19\,nC/cm^2$ equals to $-25\,mV$ in the one-dimensional semi-infinite case of a solid–fluid interface [7]. This geometry depicts all the key features in a typical microfluidic device, including the entrance and exit effects, and avoids the need to implement artificial boundary conditions at the inlet and outlet of the device. These artificial boundary conditions stem from the assumption of an infinitely long microchannel which was adopted in the simplified geometry for analytical derivation. To the extent of our knowledge, this geometry has been originally adopted by Daiguji et al. [54,55] for steady-state problems and later adapted to transient problems by Mansouri et al. [24,56].

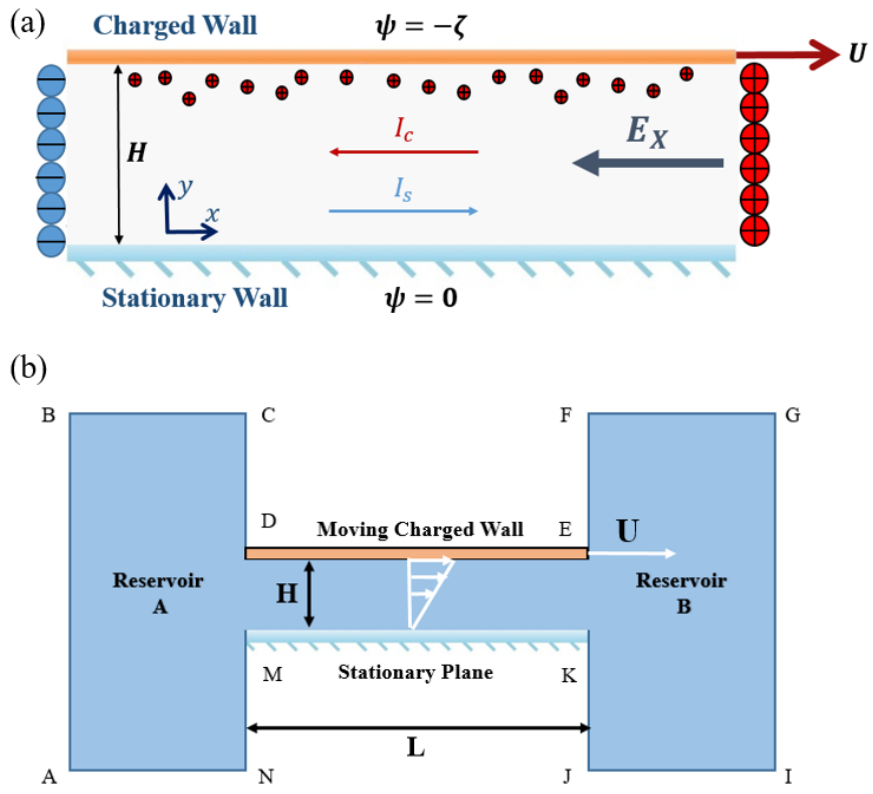

Figure 2.1 (a) Schematic of the proposed model showing the oil-water interface as a moving charged wall creating a charge buildup near the channel ends (b) Schematic for the numerical model where $L = 50\kappa H$ *and* $H = 10\kappa H$.

2.2.2 **Governing equations**

The electrokinetic flow in a shear driven slit microchannel is governed by three different types of physical models: a hydrodynamic Couette flow, electrical potential distribution and conservation of ions principle [57]. These three different types of models are coupled together allowing the development of an electrokinetic flow that induces a streaming potential and possibly a flow reversal phenomenon.

The hydrodynamic Couette flow was modeled using the Navier–Stokes momentum equations, where an electrical body force is added, as shown in Eq. (2.1) [12]:

$$\rho\left(\frac{\partial \mathbf{u}}{\partial t} + u.\nabla\mathbf{u}\right) = -\nabla p + \mu\,\nabla^2\mathbf{u} - \rho_f \nabla\psi \tag{2.1}$$

Where ρ is the fluid density, $\mathbf{u}$ is the velocity vector, μ is the viscosity, ρ_f is the charge per unit volume (free charge density) and ψ is the electrical potential. It is common to ignore the convective term $u.\nabla\mathbf{u}$ for creeping flows, which is typically the case in most microfluidic channels [58].

The electrical potential distribution was modeled using the Poisson equation highlighted in Eq. (2.2):

$$\nabla^2\psi = \frac{-\rho_f}{\varepsilon} \tag{2.2}$$

Where ε is the dielectric permittivity of the liquid. The free charge density is related to the concentration of the electrolytic solution through Eq. (2.3):

$$\rho_f = \sum z_i e n_i \tag{2.3}$$

Where z is the valence, e is the elementary charge and n_i is the ionic number concentration of the i^{th} ion in the solution.

The permittivity and all other fluid properties are assumed to be constant and uniform across the domain. This is a valid assumption for a very dilute homogenous aqueous solution which is typically the case in most microfluidic devices.

The ion conservation can be implemented using the flux conservation equation, Eq. (2.4):

$$\nabla . \boldsymbol{J_i} = 0 \tag{2.4}$$

Where $\boldsymbol{J_i}$ is the total flux for each ionic species. Ion transport, in the electrolyte solution under the effect of an electric field, is described by the Nernst–Planck equation. The total flux of ions in the solution can be represented as the vector sum of convective, diffusive and migration fluxes highlighted by Eq. (2.5):

$$\boldsymbol{J_i} = n_i \boldsymbol{u} - D_i \nabla n_i - \frac{z_i e n_i D_i}{k_B T} \nabla \Phi \tag{2.5}$$

Where D_i is the diffusion coefficient of the i^{th} species, k_B is the Boltzmann constant and T is the absolute temperature.

A list of values for the parameters used in both the analytical and numerical solutions is presented in Table 2.1.

Table 2.1 Parameter values used in the present work

Parameter	Symbol	Unit	Value
Solvent permittivity	ϵ	C^2/Nm^2	$78.54 \times 8.854 \times 10^{-12}$
Moving wall potential	ξ	mV	$-25\ to\ -250$
Dimensionless channel gap	κH	-	$10\ to\ 100$
Ion valence	z_i	-	1
Ion diffusivity	D	m^2/s	1×10^{-9}
Temperature	T	K	298
Fluid viscosity	μ	$N.s/m^2$	0.001
Magnitude of the electron charge	e	C	1.602×10^{-19}
Boltzmann constant	K_B	J/K	1.381×10^{-23}
Moving wall velocity	U	ms^{-1}	0.001

In order to optimize the size of the computational domain and to generalize our numerical solution, all the governing equations presented were non-dimensionalized using the Debye length for symmetric binary electrolytes.

The definition of the Debye length for a symmetric electrolyte is:

$$k^{-1} = \left(\frac{\epsilon K_B T}{2e^2 z^2 n_\infty}\right)^{1/2} \tag{2.6}$$

Where the scaling factors are presented in Table 2.2.

Table 2.2 Scaled parameters of the governing equations along with the scaling equations [59]

Parameter	**Non-Dimensional form**	**Relation Equation**
Axial coordinate	$\overline{x}$	κx
Vertical coordinate	$\overline{y}$	κy
Time	τ	$\kappa D^2 t$
Gradient	$\overline{\nabla}$	$\kappa^{-1}\nabla$
Pressure	$\overline{p}$	$\frac{z^2 e^2}{\epsilon\, \kappa^2 K_b^2 T^2} p$
Velocity	$\overline{\mathbf{u}}$	$\frac{1}{D\kappa}\boldsymbol{u}$
Fluid viscosity	$\overline{\mu}$	$\frac{z^2 e^2 D}{\epsilon\, K_b^2 T^2}\mu$
Fluid density	$\bar{\rho}$	$\frac{z^2 e^2 D^2}{\epsilon\, K_b^2 T^2}\rho$
Ion concentration	$\overline{n}_p, \overline{n}_n$	$\frac{n_p}{n_\infty}, \frac{n_n}{n_\infty}$
Free charge density	$\overline{\rho_f}$	$\frac{1}{zen_\infty}\rho_f$
Electric potential	$\overline{\psi}_d$	$\frac{ze}{K_b T}\psi$

The non-dimensionalized parameters were substituted into the momentum equation (Eq. (2.1)) and, with ignoring the convective term, the resulting non-dimensional form is:

$$\bar{\rho}\,\frac{\partial \overline{\mathbf{u}}}{\partial \tau} = -\overline{\nabla}\,\overline{p} + \overline{\mu}\,\overline{\nabla}^{2}\overline{\mathbf{u}} - 0.5\left(\overline{n}_p - \overline{n}_p\right)\overline{\nabla}\,\overline{\psi}_d \tag{2.7}$$

Where $\overline{n}_p$ and $\overline{n}_n$ are the scaled concentrations of the co-ions and counter-ions, respectively for a symmetric binary electrolyte solution. Moreover, the non-dimensional form of the Poisson equation is:

$$\overline{\nabla}^2\,\overline{\psi}_d = -0.5\left(\overline{n}_p - \overline{n}_p\right) \tag{2.8}$$

And finally, the non-dimensional Nernst–Plank equations for the positive and negative ions are presented by Eq. (2.9) and Eq. (2.10), respectively:

$$\frac{\partial \overline{n}_p}{\partial \tau} = -\overline{\nabla}\,.\,(\,\overline{n}_p\,\overline{\mathbf{u}} - \overline{\nabla}\,\overline{n}_p - \,\overline{n}_p\,\overline{\nabla}\,\overline{\psi}_d) \tag{2.9}$$

$$\frac{\partial \overline{n}_n}{\partial \tau} = -\overline{\nabla}\,.\,(\,\overline{n}_n\,\overline{\mathbf{u}} - \overline{\nabla}\,\overline{n}_n + \,\overline{n}_n\,\overline{\nabla}\,\overline{\psi}_d) \tag{2.10}$$

Two important points must be noted in our simulations. First is the presence of time-dependent terms in all the governing transport equations, which highlights the coupled transient dependence of the physical models involved. Second, our simulations initially start from a quiescent point at zero flow conditions and then the transient behavior of the system is traced until it has reached a steady-state flow.

2.2.3 **Boundary and initial conditions**

All the boundary conditions employed for each of the governing equations are depicted in Figure 2.2. Figure 2.2 (a) shows the boundary conditions for the Navier-Stokes equations where the flow setting is based on a flow from left to right. The inlet boundary condition (A-B) and the outlet boundary condition (G-I) were set to the same pressure to ensure that there is no pressure difference between them that can create any auxiliary flows. The flow is thus primarily caused by the slip

velocity boundary condition applied to the upper wall of the slit microchannel (D-E). The reservoir boundaries (B-C, F-G, A-N, and J-I) were assigned slip boundary condition to mimic the behavior of a semi-infinite reservoir. For all other boundaries, a no-slip boundary condition was employed to emulate the behavior of a stationary wall. With respect to the Poisson equation, as shown in Figure 2.2 (b), a scaled surface potential was applied to the upper microchannel wall (D-E). This is equivalent to having a constant charge density boundary condition applied for the upper wall in a semi-infinite solid-fluid interface. A reference potential of zero was set at the flow inlet (A-B) as this boundary represents the "bulk" conditions far from the inlet and exit of the microchannel. Zero potential gradient was applied for all other boundaries to mimic a far-field condition with no variation in the field. Finally, for the Nernst–Plank equations in Figure 2.2 (c), the inlet and outlet boundaries were assigned an electrically neutral electrolytic solute with a scaled ion concentration of 1 representing the bulk ion concentration. All other boundaries were impermeable for the ions and therefore were assigned a zero normal flux condition.

The steady-state solution of the Poisson and Nernst–Plank equations along with the no-flow quiescent state were used as the initial conditions for the transient flow simulation. This allowed us to investigate the role of ion movement and the streaming potential in forming a new equilibrium state under a steady flow condition. All our numerical results were simulated using a value of $\kappa H = 10$. This translates to the height of the channel being ten times bigger than the Debye length calculated using the values in Table 2.1Table 3.2. The scaled length of the microchannel, κL, was set to 50 while the scaled lengths of the inlet and outlet reservoirs (A-N and J-I) were assigned a value of 25. This yielded a total length of 100 for the entire microchannel and reservoirs' length (A-I) and a length to height ratio of around 5 for the microchannel. It is evident that with these dimensions the electrokinetic transport phenomena can be accurately represented [7].

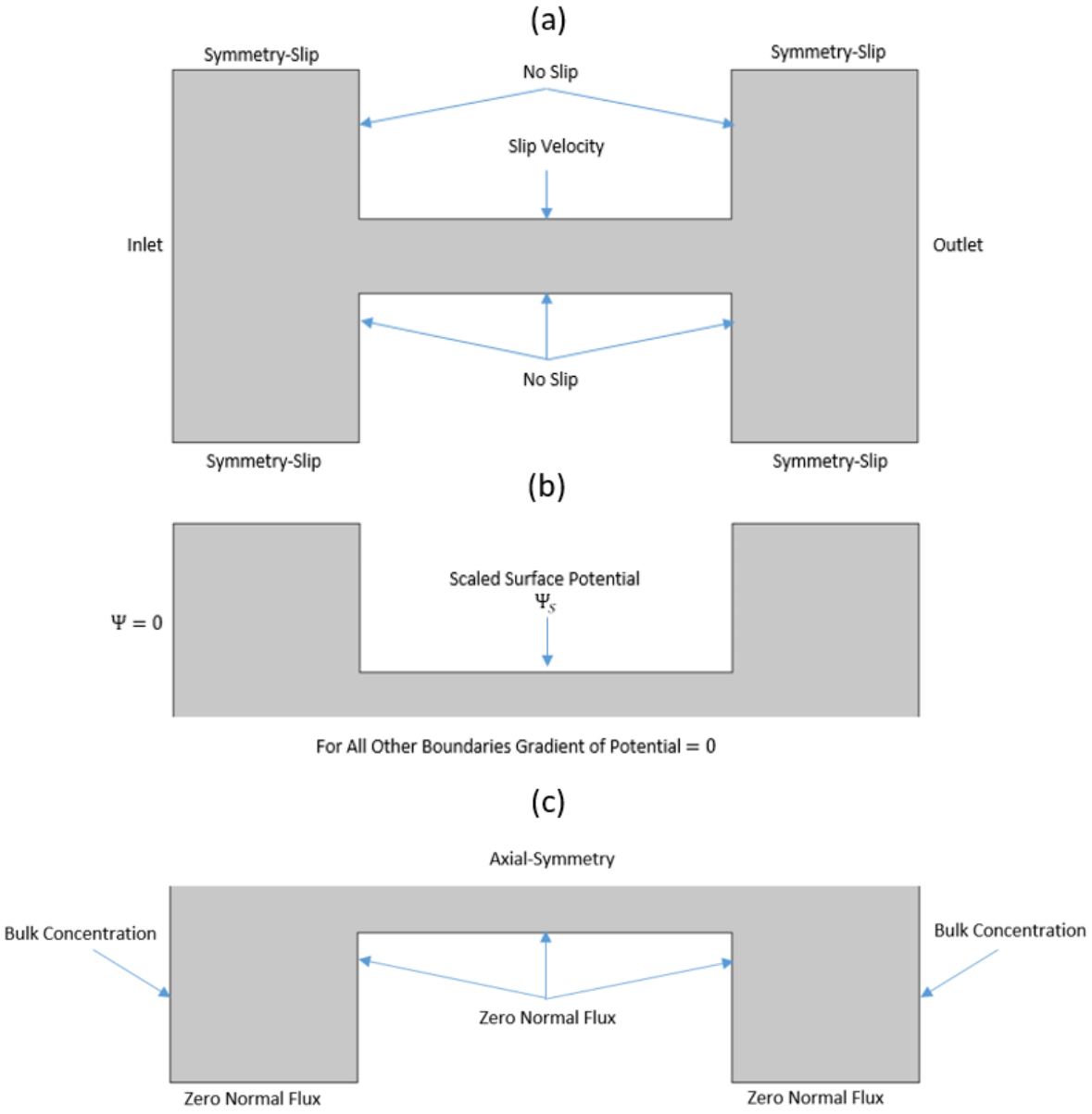

Figure 2.2. Boundary conditions for (a) momentum equation (b) Poisson equation and (c) Nernst–Plank equations.

2.3 Numerical methodology and validation

In this section, a detailed steady-state analytical model is presented. The analytical model is used to predict the evolution of streaming potential and development of an electrokinetic velocity profile

as opposed to that of a typical shear driven flow problem due to EDL effects. The analytical model predicts the flow reversal phenomenon observed for high surface potentials which will be discussed thoroughly in this section. The analytical results were validated using a transient numerical model that is also capable of determining the reformed velocity profile and the induced streaming potential. The results obtained for both models were compared to one another and all of the simplifying assumptions used in the analytical model were tested against the numerical model. The governing non-linear partial differential equations were solved using a commercial fully coupled finite element solver incorporated in COMSOL Multiphysics (V 5.3) [60]. The solution methodology involves a segregated solution method in which both the steady-state solutions for the Poisson and Nernst–Plank equations are obtained for the no-flow case in order to get the quiescent electric potential and ion distributions. After which these distributions were inputted as the initial values for the fluid flow equations in order to solve for the velocity domain. From that initial point until the steady-state condition is reached, all the four governing equations, i.e. Eqs. (7-10), were solved together in a coupled manner in order to capture the axial ion displacement within the channel which would ultimately lead to the development of the induced streaming potential. In our transient simulations, the steady-state condition is thought to be achieved when the potential difference between the two reservoirs for two consecutive time steps became almost the same to within a preset tolerance.

All the results presented in this section are mesh independent. The mesh was systematically refined until the solution became mesh independent at around 10,000 elements. All the simulations were conducted using at least 20,000 elements on a personal computer with a 4 core 3.4GHz processor and 32 GB RAM, highlighting the efficiency of the chosen computational domain. The meshing was performed using quadratic triangular elements with a finer mesh implemented as we approach

the upper wall; this is the region where the largest gradient in the electrical potential and the velocity is expected and thus the results depend highly on the number of elements near the upper wall. A second order discretization scheme was used for the velocity, electric potential and ion concentration while a first order scheme was used for the pressure. The minimum element quality used in this mesh was 0.4173. A constant newton method was used for linearization while a backward differentiation formula was used for time stepping.

2.4 Results and discussion

2.4.1 **Analytical model for high surface potentials**

In this section analytical results are presented. The analytical results were obtained for the transport of a symmetric electrolyte in a straight slit microchannel of infinite length with a surface potential on the upper wall of the channel, shown in Figure 2.1 (a). The analytical model was simplified to neglect any entrance/exit effects and axial concentration gradients. Here we summarize the key steps of the pertinent derivation.

The electric potential (Φ) at a location (x, y) is considered to be the sum of the potential due to surface charge of the microchannel wall, or simply due to the electrical double layer near the charged surface ($\psi(y)$) and the potential developed by the streaming effects ($\varphi(x)$).

$$\Phi(x,y) \equiv \psi(y) + \varphi(x) \tag{2.11}$$

$$\varphi(x) = \emptyset_0 - xE_x \tag{2.12}$$

The above superposition is valid if the variation of the electric potential in the axial direction is much smaller than the variation in the transverse direction. This can be a reasonable assumption

for a microchannel with a large aspect ratio ($L \gg H$), where L and H are the channel length and height respectively.

The motion of the ionic species in the solution is governed by the Nernst-Plank equation which at steady state is given by:

$$\nabla.\left[n_i \boldsymbol{u} - D_i \nabla n_i - \frac{z_i e n_i D_i}{k_B T} \nabla \Phi\right] = 0 \tag{2.13}$$

Applying Eq. (2.13) in the y-direction, where $u_y = 0$, results in the Boltzmann distribution for the ionic species, $n_i = n_{i_\infty} exp\big(-z_i e/K_B T\, \psi(y)\big)$ with n_∞ being the bulk ionic concentration.

$$\rho_f = e(z_+ n_+ + z_- n_-) \tag{2.14}$$

$$\rho_f = e z n_\infty (-2 \sinh(z_i e \psi / K_B T) \tag{2.15}$$

Introducing the expression for the electric potential and ionic distribution given into Poisson's equation gives the nonlinear Poisson-Boltzmann equation as:

$$\frac{d^2\psi(y)}{dy^2} = \frac{2zen_\infty}{\epsilon} sinh\left(\frac{ze}{K_B T}\psi(y)\right) \tag{2.16}$$

The boundary conditions for Eq. (2.16) are $\psi = \xi$ at $y = H$ and $\psi = 0$ and $d\psi/dy = 0$ at $y = 0$. The solution to this equation is:

$$\Psi(y) = 4\, arctanh\big(\tanh(\Psi_s/4) exp(-\kappa(H - y))\big) \tag{2.17}$$

Where κ is the inverse double layer thickness, $\kappa = (2z^2 e^2 n_\infty / \epsilon K_B T)^{1/2}$, $\Psi(y)$ and Ψ_s are dimensionless potentials defined as $\Psi(y) = ze/K_B T\, \psi(y)$ and $\Psi_s = ze/K_B T\, \xi$.

2.4.1.1 Flow velocity

In order to predict the velocity profile within the slot microchannel, additional physics had to be employed along with the Poisson-Boltzmann and Nernst-plank equations to capture the fluid flow. The flow field is governed by the modified Navier-Stokes equation including the electrical body force as:

$$0 = \mu \frac{d^2 u_x}{dy^2} + \rho_f E_x \tag{2.18}$$

Where μ is the viscosity of the electrolyte solution, u_x is the axial velocity, ρ_f is the free charge density within the liquid and $E_x = -\partial\Phi/\partial x$ is the induced electric field in x-direction. Navier-Stokes equations were implemented assuming no turbulence effects and negligible inertial effects similar to that of Stokes flow.

Making use of Poisson's equation ($\epsilon\nabla^2\Phi = -\rho_f$) along with

$$u_x(y) = \frac{1}{\mu}[\varepsilon E_x \Psi(y) + C_1 y + C_2] \tag{2.19}$$

Solving Eq. (2.19) with boundary conditions where at $y = H$, $u_x = U$ and $y = 0$, $u_x = 0$ results:

$$u(y) = U\left(\frac{y}{H}\right) + \frac{\epsilon E_x}{\mu}\left[\Psi(y) - \xi\left(\frac{y}{H}\right)\right] \tag{2.20}$$

Eq. (2.20) shows that the velocity profile consists of two main components, one is of the linear shear driven flow while the other is due to the electroosmotic backflow. In order to obtain a final expression for the electric potential and flow distributions, it is required to evaluate the induced electric field,E_x. The expression for the electric field E_x can be obtained by studying the total electric current within the liquid.

2.4.1.2 Streaming potential

The total current flow per unit width of the channel can be expressed as $I = \int_0^H i_x dy$, where the current density in the x-direction is given by:

$$i_x = eu\sum z_i n_i - e\sum D_i z_i \frac{dn_i}{dx} + \frac{e^2}{K_B T} E_x \sum z_i^2 D_i n_i \tag{2.21}$$

In the present analysis, it is assumed that there is no ion concentration gradient in the axial direction($\partial \mathrm{n_i}/\partial \mathrm{x} = 0$); hence, Eq. (2.21) can be written as $I = I_s + I_c$. The first term in the expression of the total current, $I_s = \int_0^H u\sum z_i e\, n_i dy$, referred to as the streaming current, is due to convective transport of the excess ions in the mobile double layer region (diffuse layer) near the charged interface, where the electroneutrality term $\sum z_i n_i$ is not zero. The second term,$I_C = \frac{e^2}{K_B T} E_x \int_0^H \sum z_i^2 D_i n_i \, dy$, is referred to as conduction current and is due to electric conduction through the liquid along the channel.

Assuming the same diffusion coefficient ($D_+ = D_- = D$) and bulk concentration ($n_{+\infty} = n_{-\infty} = n_\infty$) for the positive and negative ions, the conduction current can be written as:

$$I_C = 2\frac{z^2 e^2 D}{K_B T} n_\infty E_x \int_0^H \cosh\left(\frac{ze}{K_B T}\psi(y)\right) dy \tag{2.22}$$

Considering the electric conductivity σ^∞ as:

$$\sigma^\infty = 2\frac{z^2 e^2 D}{K_B T} n_\infty \tag{2.23}$$

We find that substituting Eq. (2.17) into Eq. (2.22) leads to:

$$I_C = \sigma^{\infty} E_x H \int_0^H \cosh\left(4\, arctanh\left(\tanh(\Psi_s/4) exp(-\kappa y)\right)\right) dy \tag{2.24}$$

Which can be further simplified into:

$$I_C = \sigma_{\infty} E_x H\, F_{cs} \tag{2.25}$$

In the above expression, F_{cs} is a parameter that shows the non-electroneutrality of the solution ($\sum z_i^2 n_i \neq 0$) due to the formation of the electrical double layer near the charged wall. For a more thorough understanding of the F_{cs} parameter, the electrolyte solution's conductivity changed due to the formation of an electric double layer where the new conductivity is defined by $\sigma_{FluidwithEDL} = \sigma_{\infty} F_{cs}$.

Figure 2.3 shows the variation of the F_{cs} parameter with surface potential for different κH. Figure 2.3 shows that increasing the surface potential leads to an increase in $F_{cs}'s$ value. This is because of the higher polarization effect created by increasing the surface potential of the wall. This surface potential causes more ions to build up in the electric double layer leading to more deviation from the electro-neutral state within the fluid layer. Moreover, Figure 2.3 also highlights the effect of $\kappa H, the\ Debye\ length,$ on the F_{cs} value, where F_{cs} decreases and approaches unity as κH increases. Increasing κH translates into a thin EDL which based on the relation, $\sigma_{FluidwithEDL} = \sigma_{\infty}\, F_{cs}$, means that the bulk conductivity is more dominant over the EDL conductivity. This leads to the expectation that the conductivity of the electrolyte solution tends to be the same as that of an electrolyte solution with no EDL (with an electroneutral wall).

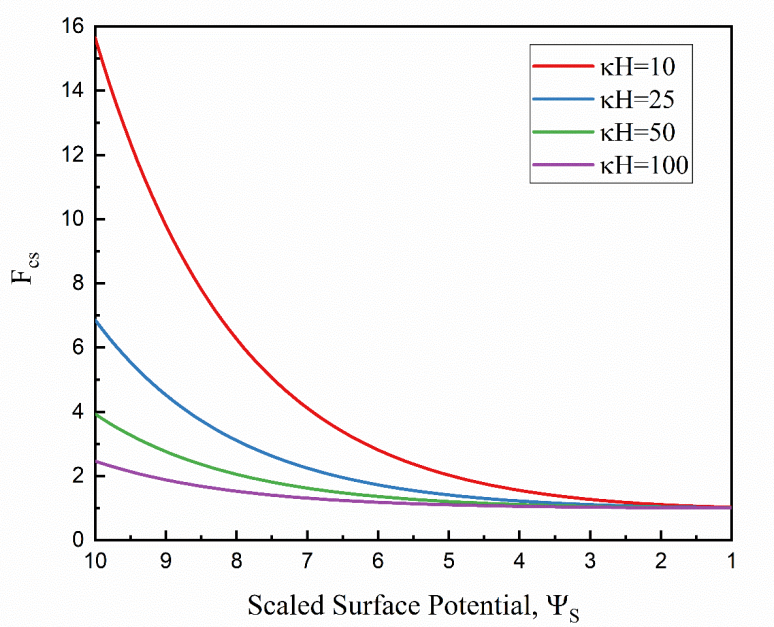

Figure 2.3 Variation of the F_{cs} with surface potential for different κH.

The streaming current can be represented as

$$I_S = \int_0^H u\left(-\epsilon \frac{d^2\psi(y)}{dy^2}\right) dy \tag{2.26}$$

For the case of streaming potential flow, the streaming and conduction current cancel out each other at steady-state resulting in a no net electric current through the liquid.

Setting total current to zero, $I = I_C + I_S = 0$, and solving for E_x give the strength of the induced electric field as:

$$E_x = -\mu U \Omega \tag{2.27}$$

Where

$$\Omega = \frac{C_1 \kappa H + \xi}{\mu D (\kappa H)^2 F_{cs} + C_2 \kappa H \epsilon - \epsilon \xi^2} \tag{2.28}$$

and the constants C_1 and C_2 are

$$C_1 = -2\left(\frac{K_B T}{ze}\right) sinh(\Psi_s/2\ ) \tag{2.29}$$

$$C_2 = 8\left(\frac{K_B T}{ze}\right)^2 sinh^2(\Psi_s/4\ ) \tag{2.30}$$

Finally, substituting the above expression for E_x in Eq. (2.20) gives the scaled local velocity field within the channel:

$$u^*(y) = \frac{u(y)}{U} = \left(\frac{y}{H}\right) - \epsilon\, \Omega\left(\psi - \xi\left(\frac{y}{H}\right)\right) \tag{2.31}$$

Eqs. (2.27—2.31) provide the conditions for the streaming potential flow. For a known applied moving wall velocity, Eq. (27) provides the axial electric field engendered by the shear-driven flow. From this field, knowing the length of the microchannel, one can determine the potential difference set up across the microchannel, which is the streaming potential.

Figure 2.4 depicts the effect of changing the non-dimensional surface potential and varying the Debye length on the induced electric field. The graph shows that for lower values of κH, which translates into a more diluted solution (higher electric double layer thickness), the induced electric field (streaming potential) increases. This could be simply explained by the fact that for a diluted solution the ionic concentration, n_∞, is lower. Since the conduction current is directly proportional to the ionic concentration, and the total current in our system must be zero at the steady-state condition $I = I_C + I_S = 0$, a higher E_x is expected in order for the conduction current to cancel out the streaming current at the steady-state condition. Moreover, increasing surface potential causes E_x to increase as well. Increasing the surface potential causes an increase in the ionic concentration of the electric double layer as shown in Figure 2.5.

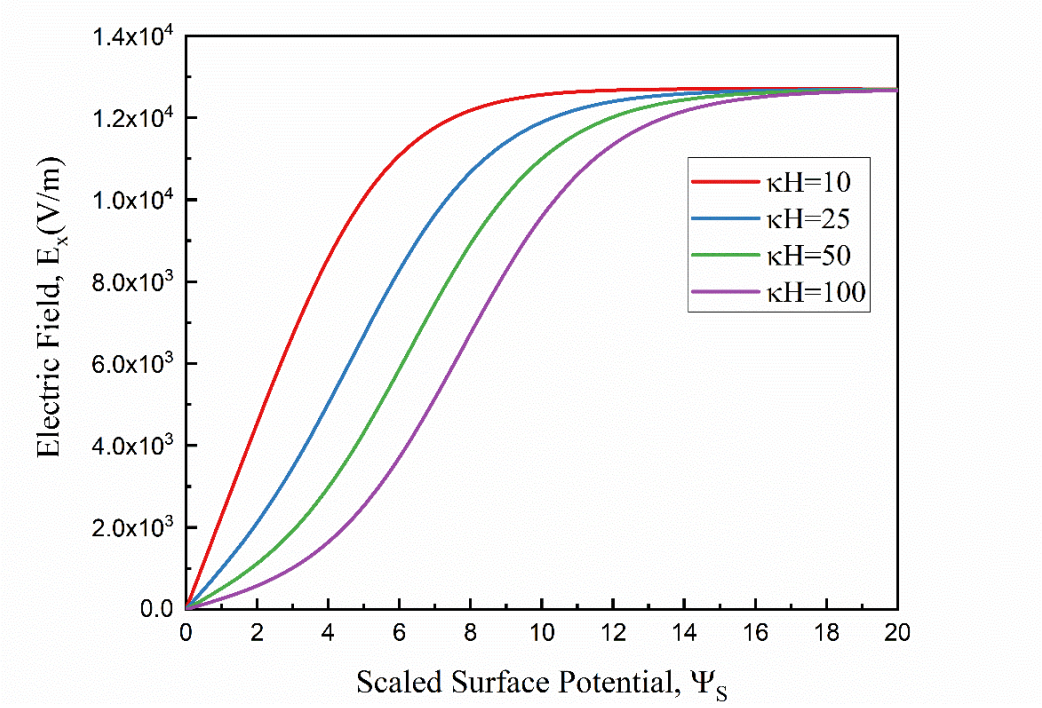

Figure 2.4 The effect of varying the non-dimensional surface potential and κH on the corresponding induced electric field.

The increase in ions in the electric double layer leads to more ions moving due to the shear driven flow. This, in turn, causes a larger buildup of ions near the ends of the channel resulting in a higher electric field. It is worth noting that in Figure 2.4 as we increase the surface potential to any value greater than 10, $\Psi_s > 10$, the electric field starts to become uniform and stable along the channel.

For a detailed explanation of this phenomenon, the ion concentration distribution and the electric double layer potential distribution for different surface potentials are presented in Figure 2.5 (a) and Figure 2.5 (b), respectively. Figure 2.5 (a) shows that as the surface potential, Ψ_s, increases, its effect on the electric potential distribution becomes less and less significant. This is clear as the shift in the electric potential distribution from $\Psi_s = 3$ to $\Psi_s = 6$ is much more substantial than that from $\Psi_s = 9$ to $\Psi_s = 12$. Consequently, since the ionic concentration distribution is highly

dependent on the electric potential distribution, Figure 2.5 (b) shows the same behavior. Similarly, as the surface potential, Ψ_s, increases, its effect on the ionic concentration distribution becomes less noteworthy (compare graphs for $\Psi_s = 9$ and $\Psi_s = 12$). Therefore, the ionic concentration in the EDL reaches a constant value regardless of the value of the surface potential, which translates into the same amount of ions buildup near the end of the channels. This behavior leads to the induced electric field becoming stable and more independent of the surface potential at values of $\Psi_s > 10$.

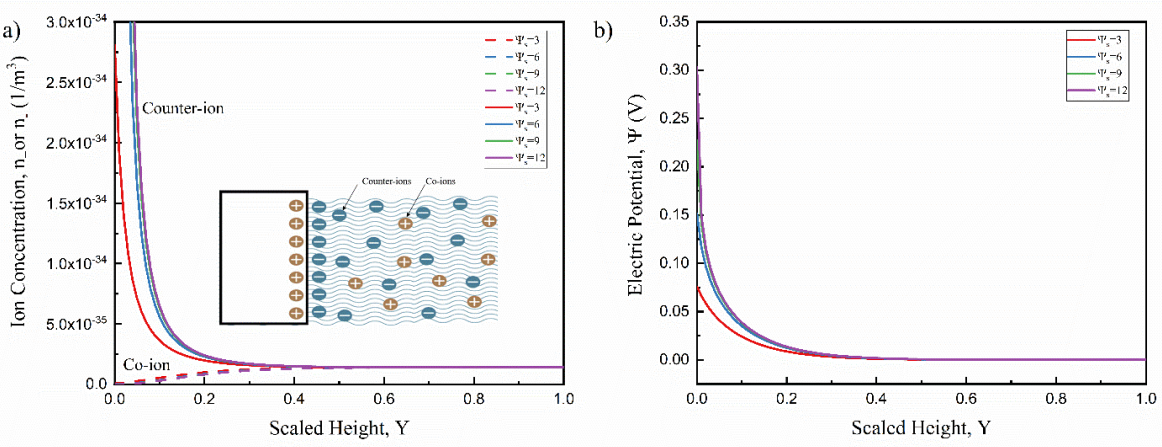

Figure 2.5 (a) the effect of different surface potential on the ionic concentration distribution along the height of the channel. (b) The effect of different surface potential on the electric potential along the height of the channel.

Figure 2.6(a) and 6(b) illustrate that the change of dimensionless flow velocity profile arises from shear stress and electroosmotic effects, respectively. From these figures, it is observed that the shear driven flow is independent of κH and exhibits a linear behavior. This behavior is that of a typical Couette flow as this is a classical lid-driven flow problem in fluid mechanics. As for the electrokinetic velocity profile, for a small surface potential of $\Psi_s = 1$, the velocity profile starts to deviate slightly from linear behavior and becomes dependent on κH value [61].

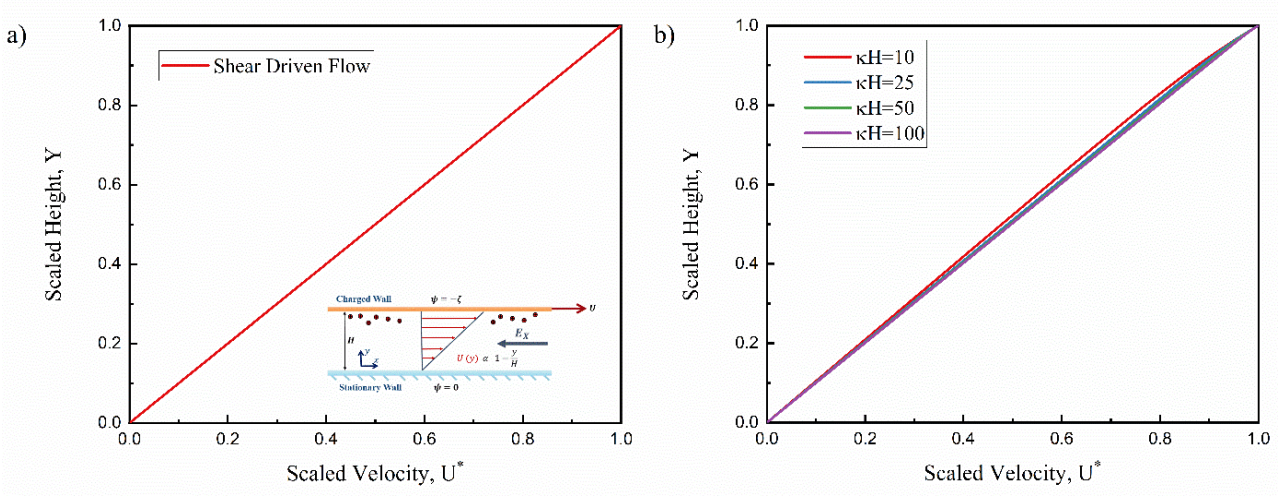

Figure 2.6 Velocity profile. (a) Shear driven velocity profile (b) Electroosmotic velocity profile.

2.4.1.3 Electro-viscous effect

The volumetric flow per unit width of the slit microchannel is given by:

$$Q = \int_0^H u_x(y)\, dy \tag{2.32}$$

Substituting Eq. (20) and performing the integration leads to:

$$Q = \frac{UH}{2} + \frac{\varepsilon E_x \zeta}{\mu}\left[\frac{-H}{2} + \frac{4\tanh(\Psi s/4)\,(1 - e^{-kH})}{k\zeta} + \frac{4\tanh^3(\frac{\Psi_s}{4})(1 - e^{-3kH})}{3k\zeta}\right] \tag{2.33}$$

Figure 2.7 (a) highlights the electroviscous effect, as discussed by Kim et al. [62]. The graph shows the impact of κH on the non-dimensional volumetric flow rate. The flow rate was scaled by the volumetric flow rate in the simple shear driven flow case with the absence of any electrokinetic effect $Q_{scaling} = \frac{UH}{2}$. The graph shows that the induced streaming potential reduces the volumetric flow rate for intermediate values of κH. This reduction in the volumetric flow rate gives the appearance of an increased viscosity for the fluid, hence the term "electroviscous effect". The fluid acts as if it has a higher viscosity because of the additional force opposing the flow. Finally, Figure

2.7 (b) shows that increasing the surface potential increases the "electroviscous effect" reducing the volumetric flow rate even more at intermediate κH values. For a surface with zeta potentials of around 75mV ($\Psi_s = 3$), the electroviscous effect can reduce the flow rate by more than 35 percent.

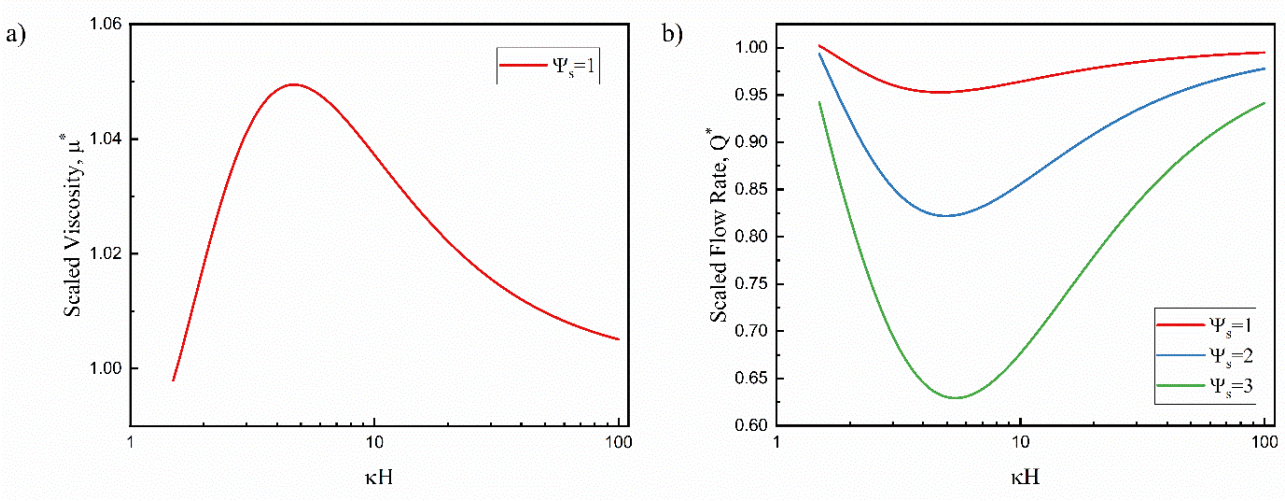

Figure 2.7 (a) A plot of normalized viscosity $\frac{\mu_a}{\mu}$ versus κh for $\Psi_S = 1$ at $\kappa H = 10$ (b) A plot of non-dimensional flow rate versus κh for different surface potentials at $\kappa h = 10$.

2.4.1.4 Flow reversal for high surface potentials

Flow reversal is a phenomenon that is observed when the electroosmotic backflow is larger than the shear driven forward flow. The electroosmotic backflow is proportional to the surface potential while the shear driven flow is proportional to the slip velocity of the moving plate. Figure 2.8 shows the different velocity profiles that can be obtained by varying the surface potential for the same slip velocity $U = 0.001\ m/s$. It is clear that as the surface potential increases, the average flow velocity decreases until $\psi_S = 5$. For scaled surface potentials greater than 5 (125 mV), the velocity profile reverses direction and we start seeing negative velocities in areas further away from the moving charged wall.

Figure 2.8 shows that increasing κH or decreasing the Debye length causes the surface potential to get screened quickly and therefore results in a lower peak that takes place in a lower position with respect to Y. Another important observation is the presence of a stationary point for situations where there is a reverse in the flow direction.

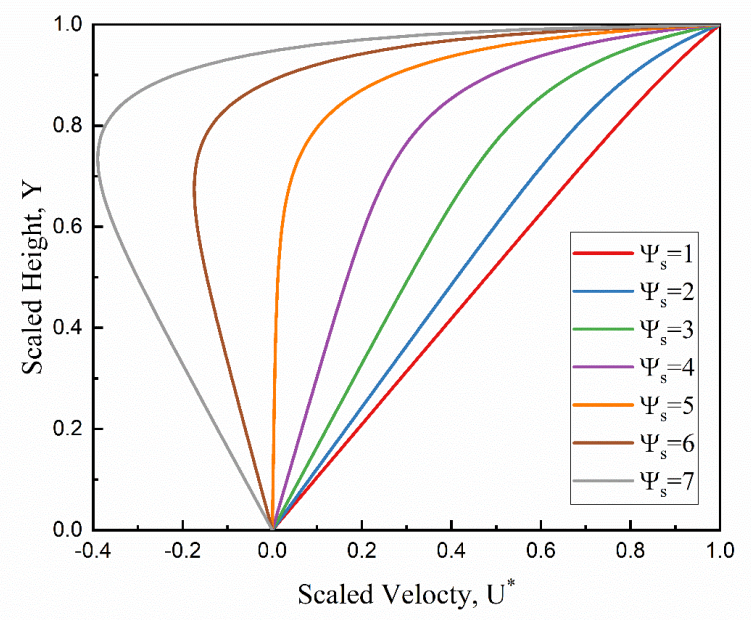

Figure 2.8 the effect of various Ψ_s on Velocity profile at κh=10.

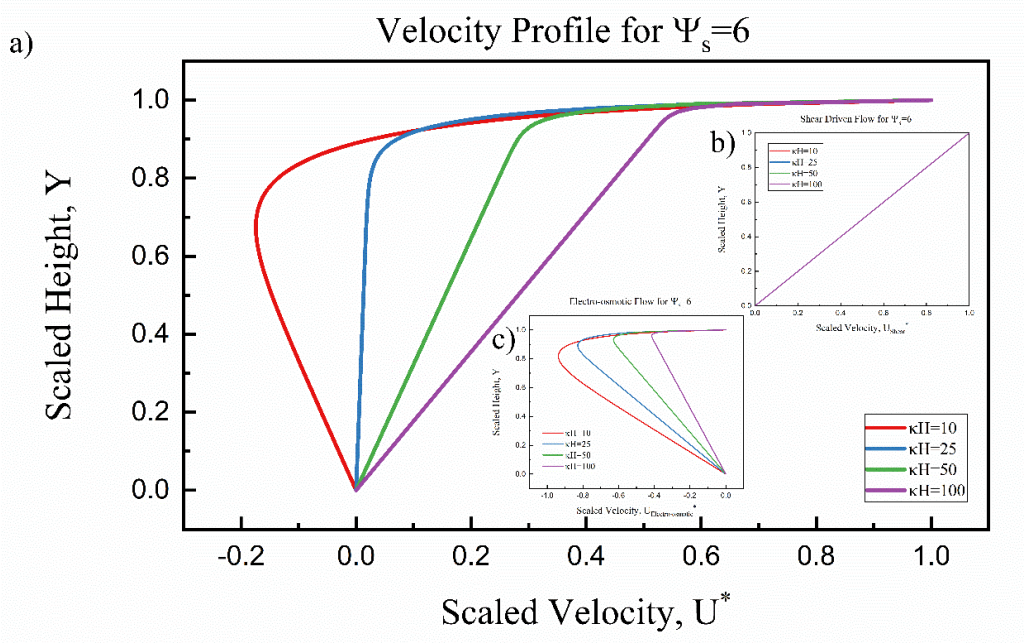

Figure 2.9 (a) The velocity profile for $\Psi_s = 6$ and different values of κH. (b) The shear driven component of the velocity profile for $\Psi_s = 6$ and different values of κH. (c) The electroosmotic velocity profile for $\Psi_s = 6$ and different values of κH.

2.4.2 **Comparison of numerical and analytical results**

2.4.2.1 Electric field

To validate the finite element formulation, we compared the predictions from the steady-state numerical model against existing analytical results for streaming potential flow in an infinitely long slit microchannel. The analytical results were obtained for the transport of a symmetric electrolyte in a straight slit microchannel of infinite length with a surface potential on the upper wall of the channel. To calculate the induced electric field over a given length of the slit microchannel using the numerical approach, the right-hand side of Eq. (2.34) was evaluated employing the same channel height, surface potential, and other conditions applied to our numerical simulations. This value of the streaming potential was employed to calculate the induced electric field E_x over the length L using:

$$E_x = \frac{\nabla\psi}{L} \tag{2.34}$$

The electric field calculated using the analytical expression, Eq (2.27), is compared with the electric field between the two reservoirs obtained from the numerical simulations, using Eq. (2.34). This comparison is done for different values of scaled surface potentials found in Figure 2.10. In our analysis, the streaming potential was measured near the centerline of the channel. Under these conditions, it can be concluded from Figure 2.10 that the numerically and analytically evaluated electric fields across the channel are in good agreement. The numerical prediction shows similar values to the analytical results for all values of surface potentials within a 15 percent margin of error.

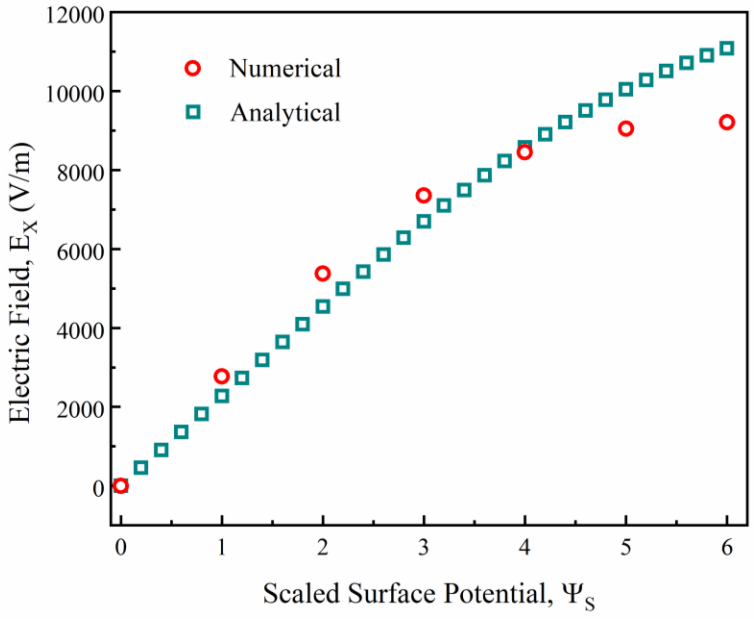

Figure 2.10 Comparison of the numerical and analytical calculations of the streaming potential for different surface potentials.

2.4.2.2 Velocity profile

The velocity profile obtained from the numerical simulations was also compared to that of the

analytical expression in Eq. (2.31). Figure 2.11 (a) shows that velocity deviates slightly from the initial behavior as time progresses. The velocity decreases as ions start to move across the channel inducing an electric field opposite to the flow. This induced electric field creates an electroosmotic backflow that opposes the shear driven flow causing a flow retardation effect. This behavior agrees with the analytical velocity profile obtained in Figure 2.9. However, it can be noted that the numerical simulation slightly overestimates the velocity reduction effect when compared to the analytical result. This can be mainly attributed to the entrance/exit effect as it is clear that at the initial time step $\tau = 0$, the velocity distribution is not perfectly linear. This linearity prediction fails because our assumption of infinitely long plates breaks down in real life microchannels making the numerical results more reliable than our simplified analytical model.

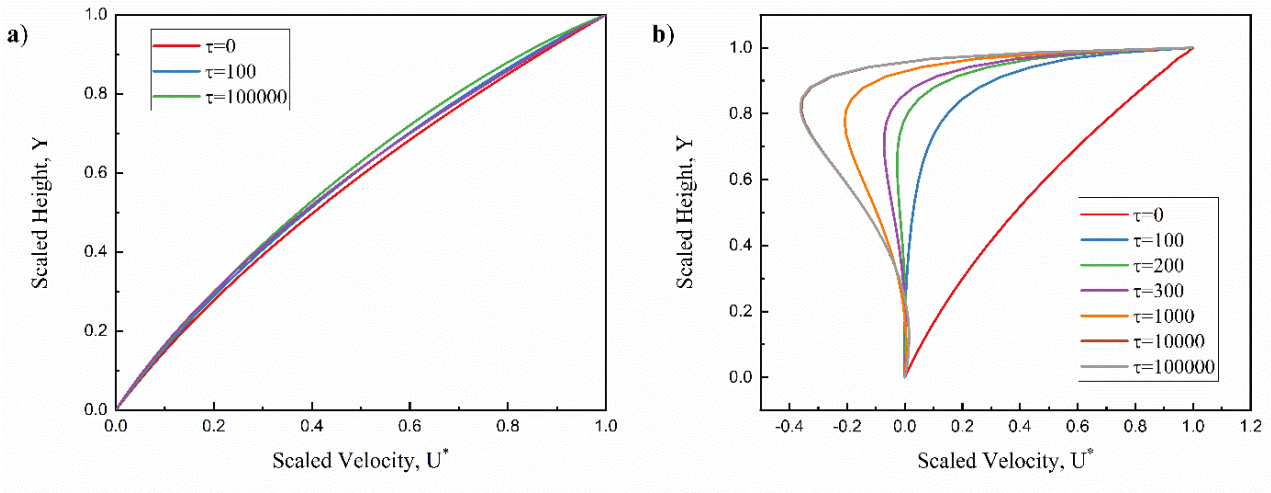

Figure 2.11 (a) Velocity Profile for $\Psi_S = 1$ (b) Velocity Profile for a $\Psi_S = 6$ showing the flow reversal phenomenon.

Figure 2.11 (b) shows the effect of having a high surface potential ($\Psi_S = 6$) on the velocity profile. Again, the numerical solution shows an agreement with the analytical results and fully captures the flow reversal phenomenon. Moreover, it shows the dynamics of the change in flow direction

and the time scale associated with this occurrence. At the initial time step $\tau = 0$, the flow is in the forward direction and follows the same trend predicted by the shear driven flow. During that initial step, there is no electroosmotic backflow as the induced electric field across the channel is nearly zero and has a no-to-negligible effect on the velocity profile. At the first time step, $\tau = 100$, the ions starts to move in the axial direction creating a buildup of positive ions in the right reservoir. This buildup creates a streaming potential that consequently induces an electric field which restrains the flow as the electroosmotic body force acting on the fluid is proportional to the induced electric field and the free charge density that occurs within the electric double layer near the wall as highlighted by Eq. (2.35). At the time steps $\tau = 200 \text{ to } 300$, the flow starts to stagnate as the electroosmotic backflow becomes almost equal to the shear driven flow in the central part of the channel. The electroosmotic flow starts to dominate over the shear driven flow in the following time steps $\tau = 10^3 \text{ to } 10^4$ and flow reversal is observed near the central part of the channel closer to the charged wall. It is clear that the time scale needed to capture the later features of the flow, such as flow reversal, is much bigger than that at the beginning (velocity reduction). This can be mainly attributed to the ion movement within the electric double layer. At the initial steps $\tau = 0 \text{ to } 300$, all the ion movement within the EDL is in the positive direction, creating more and more ion buildup at the reservoirs which induces a higher electric field, hence promoting the electroosmotic backflow. However, during the late time steps $\tau = 10^3 \text{ to } 10^4$, we start observing both ion movement in the positive and negative hydrodynamic flow directions, as the ions closer to the wall in the EDL move in the positive direction those near the end of the EDL move in the negative direction causing a slower increase in ion buildup and thus a smaller increase in the induced electric field. This process keeps on going until this complex ion movement balances out

and there becomes no longer a net ion movement in the axial direction, leading to a stable electric field and achieving the steady-state condition at $\tau = 10^5$.

$$F_{electroosmoitic} = \rho_f E_x \tag{2.35}$$

The reasonable agreement between the numerical and analytical results not only serves as a validation of the numerical model but also provides considerable insight into the development of streaming potential across the slit microchannel. First, the comparison of the two solutions was performed based on conditions, particularly the velocities, determined at the mid-section of the channel. Secondly, the streaming potential in the analytical solution was based solely on the streaming and conduction current, whereas in the numerical calculations it was obtained considering all three modes of ion transport (convection, diffusion and migration). It is interesting to note that in the numerical simulation a considerable diffusive flux exists in the axial direction owing to the ion concentration differences between the two reservoirs across the channel. Plots of the pressure distribution and the recirculation streamlines can be found in the Appendix.

2.4.3 **Development of streaming potential: transient analysis**

2.4.3.1 Streaming potential and ion concentration

This section will primarily focus on how the electrokinetic flow is developed beginning from an initial quiescent state after applying the moving wall boundary condition. As explained in Section 2.2, the Poisson–Nernst–Planck equations are initially solved using the no-flow condition to get the initial stationary electric potential and ion concentration distribution. The results presented in this section will be for the case of constant interfacial charge density corresponding to an interfacial electric potential of -1. Both the streaming potential and axial ion concentration exhibit similar behavior for both high and low interfacial potential and therefore only the case for low surface

interfacial is presented here. After solving for the initial distributions, the transient Navier–Stokes equations were solved coupled with Poisson–Nernst–Planck equations beginning from an initial no-flow condition. The transient analysis was performed using a diffusion-based time scale $\tau = \kappa D^2 t$ where t is the dimensional time. For the parameters used in our simulation, $10\,\mu s$ corresponds to around $\tau = 1$. One could also nondimensionalize the governing using a hydrodynamic-based time scale $\tau = \frac{\mu}{\rho H^2}$ where $\tau = 1$ would correspond to around $25\,\mu s$. However, it more convenient to use this diffusion-based timescale in our simulations as it would enable us to capture both the evolution of electrochemical transport variables as well as the hydrodynamic variables.

Figure 2.12 depicts the predictions of the numerical model spanning the initial stages of the evolving electrokinetic flow. Figure 2.12 (a) depicts the scaled axial variation of the electric potential while Figure 2.12 (b) depicts the scaled co-axial concentrations along the centerline of the channel where the solid lines represent the counter ions concentration while the co-ions are represented by the dashed lines. The red line represents the initial state for both the electrical potential and the ion concentration. At the initial state, the electrical potential is almost constant across the channel as there is no axial variation of ions. Figure 2.12 (a) shows the electrical potential having a constant negative value at the initial state which could be attributed to the negative surface potential applied at the upper wall. This surface potential wouldn't have been fully screened at the center of the channel as it is still quite close to the wall ($y = 5\kappa h$) creating this slight negative bump. Moreover, Figure 2.12 (b) shows that at the initial state the co-ions are less than bulk concentration ($\frac{n}{n_\infty} = 1$) while counter ions are greater than the bulk implying that center of the channel experience the same behavior as that in the EDL. This agrees with the

previous observation that surface potential hasn't been fully screened at the surface of the channel. As time progresses, one could observe the development of the streaming potential across the channel. It can be also observed how the streaming potential at the first-time step $\tau = 100$, the streaming potential reaches half of its steady value while at the second time $\tau = 200$, the streaming potential increases significantly less. This decrease in the rate of development of streaming potential could be assigned to electrokinetic effects impacting the flow velocity leading to a reduction in the overall flow rate as shown in the previous section. Another factor would be the development of a backward conduction current limiting the ionic buildup near the ends of the channel which is the primary root behind the development of the streaming potential. This is confirmed by Figure 2.12 (b) as it shows the positive ions accumulating near the exit of the channel while the negative ions are more abundant towards the entry. This variation in the axial ion concentration is what eventually leads to the rise of streaming potential. Figure 2.12 (c) shows a contour plot of co-ion concentration giving us a better image of the process.

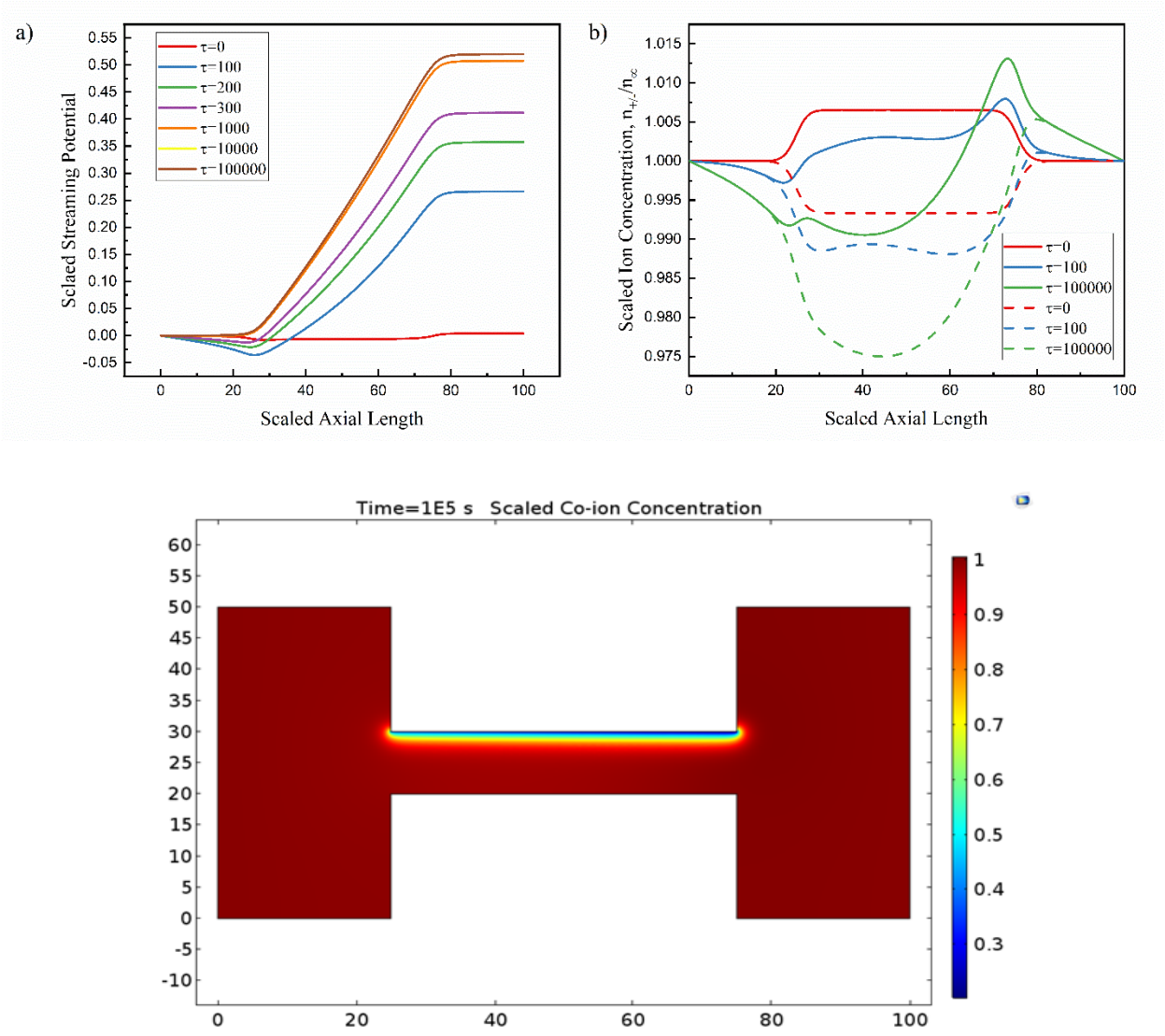

Figure 2.12 (a) Development of streaming potential across the channel (b) Scaled ion concentration across the channel where the dashed line is for the co-ion concentration while the solid lines are for the counter-ion concentration at the centerline (c) Contour plot of a scaled counter ion concentration.

2.5 Concluding remarks

In this paper, analytical expressions as well a numerical model were proposed to model two-phase flows, i.e. oil and water, in microchannels where the interfacial charge plays an important role in determining the overall velocity profile. The proposed model consists of an aqueous solution

between a moving plate and a stationary wall, where the moving plate represents the mobile charged oil-water interface. The results show that the interfacial charge of the moving interface significantly impacts the velocity profile of the flow and can reverse its overall direction. Both numerical and analytical models agree that flow reversal takes place when the interfacial potential exceeds 120 mV.

Moreover, other features concerning the induced streaming potential were examined. Our analytical analysis provides a detailed understanding of the characteristics of the two-phase streaming potential flow. The model shows the dependence of the streaming potential on both Debye's length and the interfacial charge density. It also demonstrates the reduction in the overall flow rate due to electroviscous effects. Finally, the numerical model shows the transient development of the streaming potential filling the gap that is present in the literature regarding two-phase microfluidic flows.

Chapter 2

3 Investigating Magnetic Fields of Electrokinetic Flows in Microchannels

3.1 Introduction

Microfluidic devices have become widely popular over the past decade in the area of biomedical and chemical analysis due to their advantageous properties [34,63–66]. Transporting liquids in microfluidic devices and nanofluidic devices can be mainly achieved by either a pressure gradient or an external electric field, i.e., pressure-driven flow or electroosmotic flow [67].

In microfluidic devices, channel walls develop electrostatic charges on their surface when they come into contact with an aqueous electrolyte solution. This causes the free ions in the solution to attach to the charged surface forming a layer of immobile counterions, called the Stern layer, followed by a diffuse layer of mobile ions [12,68]. Together these two layers form what is known as the electric double layer whose thickness is described by the Debye-Huckel equation. In electroosmotic flows, the external applied electrical field creates a force on the excess counter-ions in the diffuse layer, which leads to the flow of the bulk liquid due to viscous effects. The Electroosmotic flow usually has a plug-like velocity profile in microfluidic devices where the thickness of the electric double layer is several times smaller in magnitude than that of the channel's dimensions. This velocity profile can be obtained using the Helmholtz-Smoluchowski theory. However, if the dimensions of the channel are in the nanoscale and are comparable to the thickness of the electric double layer, then the electric double layer from opposite channel walls may overlap and the plug-like velocity profile is no longer valid [13]. Electroosmotic flow in nanoscale channels has been analyzed both analytically [69] and experimentally [70] and the velocity profile has been determined and correlated to the migration of ions for different channel lengths and electrolyte solutions. These studies also relate the electric double layer thickness to the mechanism of ions transport. For thick electric double layers the transport is dominated by buffer cations while for thin electric layers it is caused by neutral/anion particles. Kuang et al

presented a detailed analysis of the transient effects of electroosmotic flow in a microcapillary [27]. Yang et al discussed the time-enhanced effects of electroosmotic flow within slit microchannels [28]. They derived the analytical solutions for the fully developed laminar electrokinetic flow of liquids subjected to an applied voltage. Rice et al. also studied the analytical solution for the current distribution in microcapillaries for different channels and electrical double layer lengths [29].

These analytical studies of current and magnetic field distributions inside electroosmotic flow driven devices led to the use of solid-state charged nanopores in breakthrough applications, such as DNA sequencing, genetics' research and biomedical analysis [30–34]. The ionic currents and magnetic fields generated from the flow of single charged biomolecules, e.g., DNA, RNA and proteins, through the nanopore due to the applied electric potentials can be used to generate a distinctive electronic signal. These signals can be used for direct label-free sequencing of biomolecules. However, current research trends revolve around trying to reduce the translocation velocity in order to allow for more accurate sensing of DNA molecules [35,36]. Mansouri et al. proposed a numerical model to evaluate the internal and external magnetic field strength in charged nanochannels for the cases of pressure-driven streaming potential flows [24,71]. They also investigated the use of electromagnetic sensing tools to produce secondary non-invasive electronic signatures of biomolecules to improve the current DNA sequencing technology. However, many aspects regarding streaming potential and electroosmotic flows in small nanochannels are not well-understood, such as the transient effects of the current distributions and its relation to the generated magnetic fields.

In this paper, we propose a numerical model to evaluate the transient effects of internal and external magnetic field strength in charged nanochannels for the cases of electroosmotic flows and

shear-driven streaming potential flows. We also investigate the use shear driven flows to lower the translocation velocity which will improve the system's capability to differentiate between short length DNA and RNA molecules without sacrificing the capture rate or signal-to-noise ratios [72,73].

In order to analyze electrokinetic flows inside nanochannels, the hydrodynamics of the electrolyte solution along with the transport of ions by diffusion, convection and migration must be solved in a coupled manner [54,74–76]. The transport of ions within the nanochannels leads to current flows that generate magnetic fields both inside and outside the channel. In order to correctly simulate this model, the following partial differential equations are solved together for the electrolyte continuum to capture the physics of the problem: a) the Navier-Stokes equation for the fluid flow b) Poisson-Nernst-Planck equations for the electrical potential distribution and ion transport and c) Ampere-Maxwell's law for the associated magnetic field. The main objectives and novelty of our work can be summarized as follows: a) construct a model for transient electrokinetics for electroosmotic flows in a charged nanocapillary channel using the described system of equations, b) construct a model for the transient electrokinetic effects inside a charged nanopore for a shear driven streaming potential flow inside a slit microchannel using the same system of equations and c) evaluate the transient effects of ionic currents and the magnetic field generated both inside and outside the microchannel and compare these results with known analytical solutions for verification purposes.

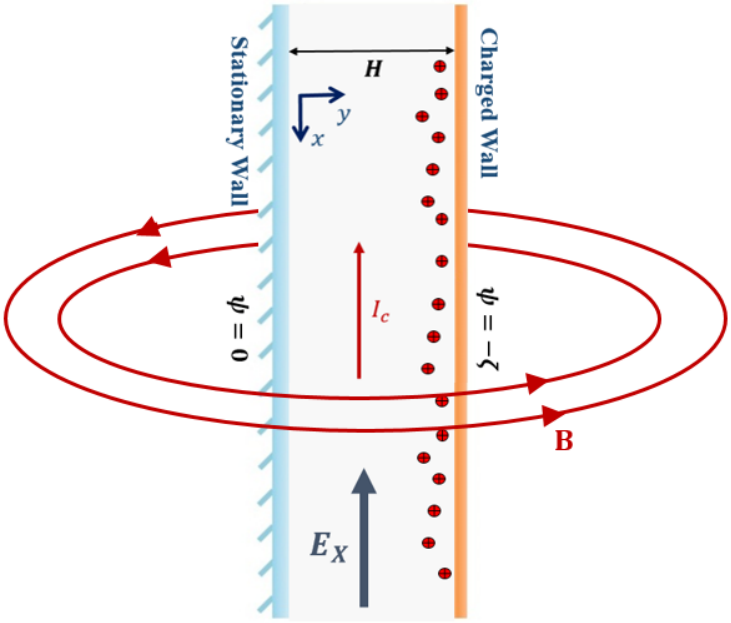

Figure 3.1 Schematic of the proposed model showing the oil-water interface as a moving charged wall creating a charge buildup near the channel ends.

3.2 Problem statement

Due to an applied electric field or a shearing motion, the mobile free ions in the electric double layer near the walls of the capillary experience a force causing them to move and generate an ionic current and consequently a magnetic field, as shown in Figure 3.1. Analytical expressions along with a numerical model for the induced current and magnetic field are presented in the subsequent sections.

3.2.1 **Geometry**

The geometries implemented in our numerical model are presented in Figure 3.2 and Figure 3.3. It consists of a microchannel of length L and height H that can be either a slit or a capillary connecting two reservoirs, where the bulk conditions of the aqueous solution dominate. The

aqueous electrolyte solution flows from one reservoir to the other due to the applied driving force. The walls of the microchannel are treated as a dielectric material having a surface charge that corresponds to a surface potential of $-0.19\,nC/cm^2$ and a zeta potential of $-25\,mV$ in the one-dimensional semi-infinite case of a solid-fluid interface [7]. The microchannel is surrounded by a domain of air used to evaluate the induced magnetic field outside the microchannel. Both geometries include all the necessary features in a typical microfluidic device and its surrounding environment, including the entrance and exit effects, and avoids the need to implement artificial boundary conditions at the inlet and outlet of the device. To the extent of our knowledge, this geometry has been originally adopted by Daiguji et al. [54,55] and by Mansouri et al. [24,56] .

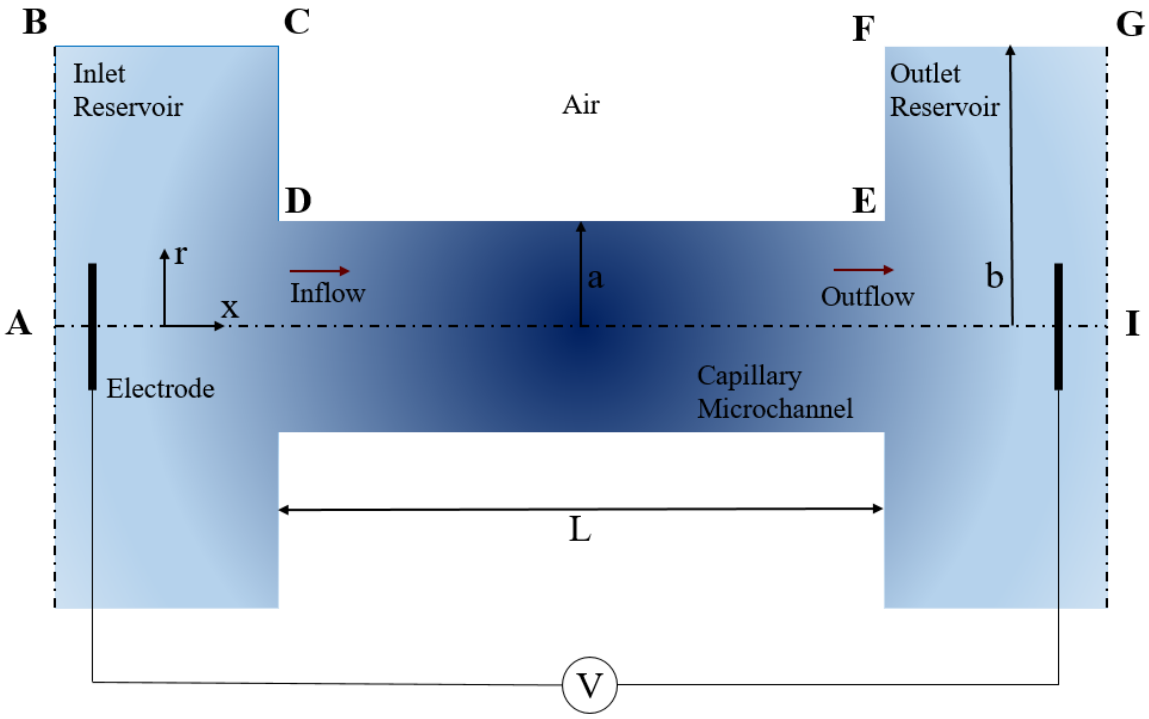

Figure 3.2 Schematic of the proposed model for electroosmosis in nanocapillary channels.

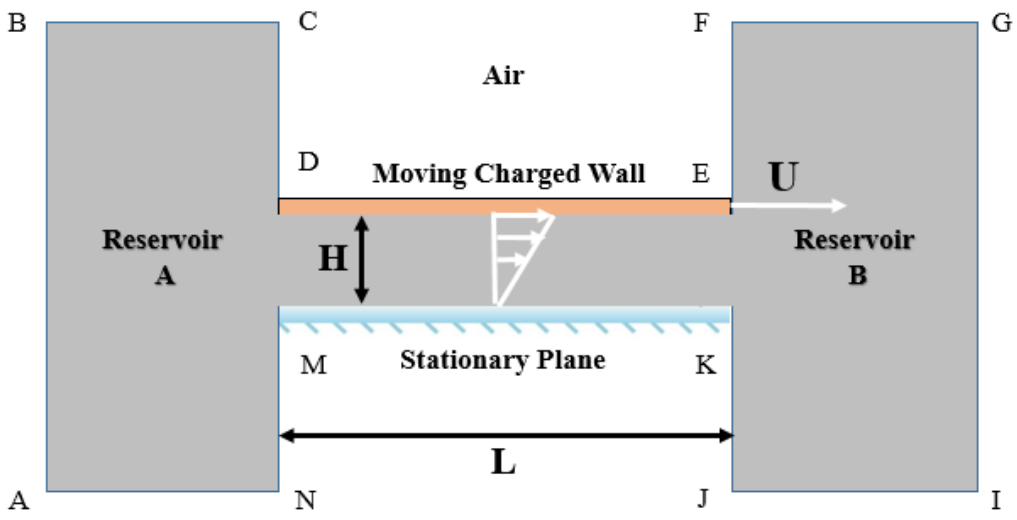

Figure 3.3 Schematic for the numerical model for a shear-driven slit microchannel.

3.2.2 **Governing equations**

The magnetic electrokinetic problem is governed by four different equations: a hydrodynamic flow, an electrical potential distribution, electromagnetics and conservation of ions physics [57]. These four different types of equations are solved together in a coupled manner to allow the development of an ionic current flow that induces a magnetic field distribution inside and around the microchannel.

The hydrodynamic problem can be modeled using the continuity and momentum equations, more specifically the Navier–Stokes equations, where an electrical body force is added, as shown in Eq. (3.1) [12]:

$$\rho\left(\frac{\partial \mathbf{u}}{\partial t} + u.\nabla\mathbf{u}\right) = -\nabla p + \mu\,\nabla^2\mathbf{u} - \rho_f \nabla\psi \tag{3.1}$$

Where ρ is the fluid density, $\mathbf{u}$ is the velocity vector, μ is the viscosity, ρ_f is the charge per unit volume (free charge density) and ψ is the electrical potential. It is common to ignore the convective

term $u.\nabla\mathbf{u}$ for low Reynolds number flows, which is typically the case in most microfluidic channels [58].

The electrical potential distribution was modeled using the Poisson equation highlighted in Eq. (3.2):

$$\nabla^2\psi = \frac{-\rho_f}{\varepsilon} \tag{3.2}$$

Where ε is the dielectric permittivity of the liquid. The free charge density is related to the concentration of the fluid through Eq. (3.3):

$$\rho_f = \sum z_i e n_i \tag{3.3}$$

Where z is the valence, e is the elementary charge and n_i is the ionic number concentration of the i^{th} ion in the solution.

The permittivity and all other fluid properties are assumed to be constant and uniform across the domain. This is a valid assumption as we are typically dealing with a very dilute homogenous aqueous solution in most microfluidic devices.

The ion conservation can be implemented using the flux conservation equation, Eq. (3.4):

$$\nabla.\boldsymbol{J_i} = 0 \tag{3.4}$$

Where $\boldsymbol{J_i}$ is the total flux for each ionic species. Ion transport, in the electrolyte solution subjected to induced electrical fields, is described by the Nernst–Planck equation. The total flux of ions in the solution can be represented as the vector sum of convective, diffusive, and migration fluxes highlighted by Eq. (3.5):

$$\boldsymbol{J_i} = n_i\boldsymbol{u} - D_i\nabla n_i - \frac{z_i e n_i D_i}{k_B T}\nabla\Phi \tag{3.5}$$

Where D_i is the diffusion coefficient of the i^{th} species, k_B is the Boltzmann constant, and T is the absolute temperature.

Magnetic fields are induced when there is a flow of ions or electrons or due to the presence of a time-varying electric flux density. In electroosmosis and streaming potential phenomena, the ionic currents that flow within these nanochannels generate magnetic fields both inside and outside the nanochannel. The Ampere-Maxwell law, used in our simulation, relates the curl of the magnetic field strength, **H**, to the ionic current density and time-changing magnetic field as shown in Eq. (3.6). The magnetic flux density, **B**, relates to magnetic field strength by, $= \mu_0\mu_r \mathbf{H}$, where μ_r is the relative permeability of air and μ_0 is the permeability of free space.

$$\nabla \text{X } \mathbf{H} = \sum e \boldsymbol{J_i} + \varepsilon \frac{\partial \boldsymbol{E}}{\partial t} \tag{3.6}$$

For the shear driven flow phenomena, there are two cases that need to be considered. The first case is the streaming current mode where the two reservoirs are electrically connected with one another by a short circuit. This essentially means that the electrical potential is the same in both reservoirs and therefore no streaming potential can be generated. This is experimentally attainable by placing two electrodes in the reservoirs and connecting them by an electrical wire. This will prevent charge build-up in the reservoirs and consequently prevent inducing a flow-induced electric field as any charge imbalance will lead to chemical reactions at the electrodes. The second case is that of the streaming potential mode that we discussed in the first chapter of our work. In this mode, the two reservoirs are not electrically connected which leads to an axial variation of charge density generating a flow-induced electric field. This leads to a conduction current that is equal but opposite in magnitude to flow-induced current leading to a null net current. The total flux of ions in the streaming potential mode is given by $\boldsymbol{J} = (n_P - n_n)\boldsymbol{u} + \frac{(n_P - n_n)D}{k_B T}\nabla\Phi$, while in the streaming

current mode it is given by $\boldsymbol{J} = (n_P - n_n)\boldsymbol{u}$, where n_P, n_n are the ionic number concentration for positive and negative ions, respectively.

In order to optimize the size of the computational domain and to generalize our numerical solution, all the governing equations presented were non-dimensionalized using the Debye length for symmetric binary electrolytes.

The definition of the Debye length for a symmetric electrolyte is:

$$k^{-1} = \left(\frac{\epsilon K_B T}{2e^2 z^2 n_\infty}\right)^{1/2} \tag{3.7}$$

Where the scaling factors are presented in Table 3.1.

Table 3.1 Scaled parameters of the governing equations along with the scaling equations [47]

Parameter	Non-Dimensional form	Relation Equation
Axial coordinate	$\overline{x}$	κx
Vertical coordinate	$\overline{y}$	κy
Time	τ	$\kappa^2 Dt$
Gradient	$\overline{\nabla}$	$\kappa^{-1}\nabla$
Velocity	$\overline{\mathbf{u}}$	$\frac{1}{D\kappa}\boldsymbol{u}$
Fluid viscosity	$\overline{\mu}$	$\frac{z^2 e^2 D}{\epsilon K_b^2 T^2}\mu$
Fluid density	$\bar{\rho}$	$\frac{z^2 e^2 D^2}{\epsilon K_b^2 T^2}\rho$
Ion concentration	$\overline{n}_p, \overline{n}_n$	$\frac{n_p}{n_\infty}, \frac{n_n}{n_\infty}$
Free charge density	$\overline{\rho_f}$	$\frac{1}{zen_\infty}\rho_f$
Electric potential	$\overline{\psi}_d$	$\frac{ze}{K_b T}\psi$
Electric Field	$\overline{E}_x$	$\frac{ze\ E_x}{K_b T\kappa}$
Magnetic Field Strength	$\bar{H}$	$\frac{1}{zen_\infty D}H$
Magnetic flux Density	$\bar{B}$	$\frac{ze\ D}{K_b T}B$
Current	$\bar{I}$	$\frac{\kappa}{zen_\infty D}I$

Current Density	$\bar{J}$	$\frac{1}{zen_{\infty}D\,\kappa}J$

The non-dimensionalized parameters were substituted into the momentum equation (Eq. (3.1)) and, with ignoring the convective term, the resulting non-dimensional form is:

$$\bar{\rho}\,\frac{\partial\overline{\mathbf{u}}}{\partial\tau} = -\overline{\nabla}\,\overline{p} + \overline{\mu}\,\overline{\nabla}^{2}\overline{\mathbf{u}} - 0.5\left(\overline{n}_p - \overline{n}_p\right)\overline{\nabla}\,\overline{\psi}_d \tag{3.8}$$

Where $\overline{n}_p$ and $\overline{n}_n$ are the scaled concentrations of the co-ions and counter-ions, respectively. The term comes from the assumption of the symmetric binary electrolyte solution, which will be explained more thoroughly in the following section.

The non-dimensional form of the Poisson equation is:

$$\overline{\nabla}^{2}\,\overline{\psi}_d = -0.5\left(\overline{n}_p - \overline{n}_p\right) \tag{3.9}$$

The non-dimensional Nernst–Plank equations for the positive and negative ions are presented by Eq. (3.10) and Eq. (3.11), and the non-dimensional Ampere-Maxwell equation is presented by Eq. (3.12), respectively:

$$\frac{\partial\overline{n}_p}{\partial\tau} = -\overline{\nabla}\,.\,(\,\overline{n}_p\,\overline{\mathbf{u}} - \overline{\nabla}\,\overline{n}_p - \,\overline{n}_p\,\overline{\nabla}\,\overline{\psi}_d) \tag{3.10}$$

$$\frac{\partial\overline{n}_n}{\partial\tau} = -\overline{\nabla}\,.\,(\,\overline{n}_n\,\overline{\mathbf{u}} - \overline{\nabla}\,\overline{n}_n + \,\overline{n}_n\,\overline{\nabla}\,\overline{\psi}_d) \tag{3.11}$$

$$\overline{\nabla}\,X\;\overline{\mathbf{H}} = \,\sum\overline{\boldsymbol{I}_{\boldsymbol{\iota}}} + 0.5\frac{\partial\overline{\mathbf{E}}}{\partial\tau} \tag{3.12}$$

Two important points must be noted in our simulations. First is the presence of time-dependent terms in all the governing transport equations, which highlights the coupled transient dependence

of the physics involved. Second is that the system's transient behavior is traced until it has reached steady-state flow conditions from a starting quiescent point at no-flow conditions.

A list of values for the parameters used in both the analytical and numerical solutions is presented in Table 3.2.

Table 3.2 Parameter values used in the present work

Parameter	Value/Range
Solvent permittivity, ϵ	$78.54 \times 8.854 \times 10^{-12}\ C^2/Nm^2$
Moving wall potential, ξ	$-25\ mV$
Dimensionless channel gap, κH	$10\ to\ 100$
Ion valence, z_i	1
Ion diffusivity, D	$1 \times 10^{-9} m^2/s$
Temperature	$298\ K$
Fluid viscosity, μ	$0.001\ N.s/m^2$
Electric Field Strength, E_x	$2.6695 \times 10^3\ V/m$
Magnitude of the electron charge, e	$1.602 \times 10^{-19}\ C$
Boltzmann constant, K_B	$1.381 \times 10^{-23}\ J/K$
Moving wall velocity, U	$0.001\ ms^{-1}$
Vacuum permeability, μ_0	$4\pi\ \times\ 10^{-7}\ \mathrm{N/A^2}$
Relative permeability of air, μ_r	1

3.2.3 **Boundary and initial conditions**

The boundary conditions employed for electroosmosis are described in Figure 3.4. Due to axial symmetry, only half of the domain is considered to correctly model the problem. Figure 3.4 (a) shows the boundary conditions for the Navier-stokes equation where the electrolyte solution flows from left to right. The inlet and outlet boundaries (A-B and G-I) are set to the same pressure so there is no pressure difference; this allows us to model the purely electroosmotic flow case. The reservoir boundaries (B-C and F-G) were assigned slip boundary conditions to mimic the behavior

of semi-infinite reservoirs. All other wall boundaries are assigned a no-slip boundary condition. Figure 3.4 (b) describes all the boundary conditions employed for the Poisson equation. The walls of the nanochannel (C-D, D-E and E-F) were set to a scaled surface potential of 1, which is equivalent to a zeta potential of 25mV. The outflow boundary is set at a reference potential of zero while the inflow boundary is set at a specified potential of 1. This is equivalent to applying a scaled electric field of 0.01 in the axial direction. Figure 3.4 (c) depicts the boundary conditions for the Nernst–Plank equations. The inlet and outlet boundaries (A-B and G-I) were assigned an electrically neutral electrolytic solute with a scaled ion concentration of 1, representing the bulk ion concentration. All other boundaries were impermeable for the ions and therefore were assigned a zero normal flux condition. For all three governing equations, axial symmetry was imposed on the boundary AI.

As for the shear-driven streaming potential case, the boundary conditions applied are described in chapter 1 of our work. The only major difference is for the electrical boundary condition at the exit outflow boundary (G-I), which is done to differentiate between the cases of the streaming current and the streaming potential modes. The electric potential of the outflow boundary was set to zero electric potential to simulate the streaming current mode, while the zero electric potential gradient was used in the streaming potential case. In electroosmosis, the inflow boundary was set to a specified potential while the outflow boundary was set to zero to mimic an applied electric field using two flat electrodes.

The steady-state solution of the Poisson and Nernst–Plank equations for the no-flow quiescent state were used as the initial conditions for the transient flow simulation. The numerical results were simulated using a capillary radius that is five times bigger than the Debye length, $\kappa a = 5$. The scaled lengths of the inlet and outlet reservoirs were assigned a value of 25 while the scaled

length of the capillary, κL, was set to 50. This yielded a total length of 100 for the entire microchannel and reservoirs' length (A-I), and a length to height ratio of ~5 for the microchannel.

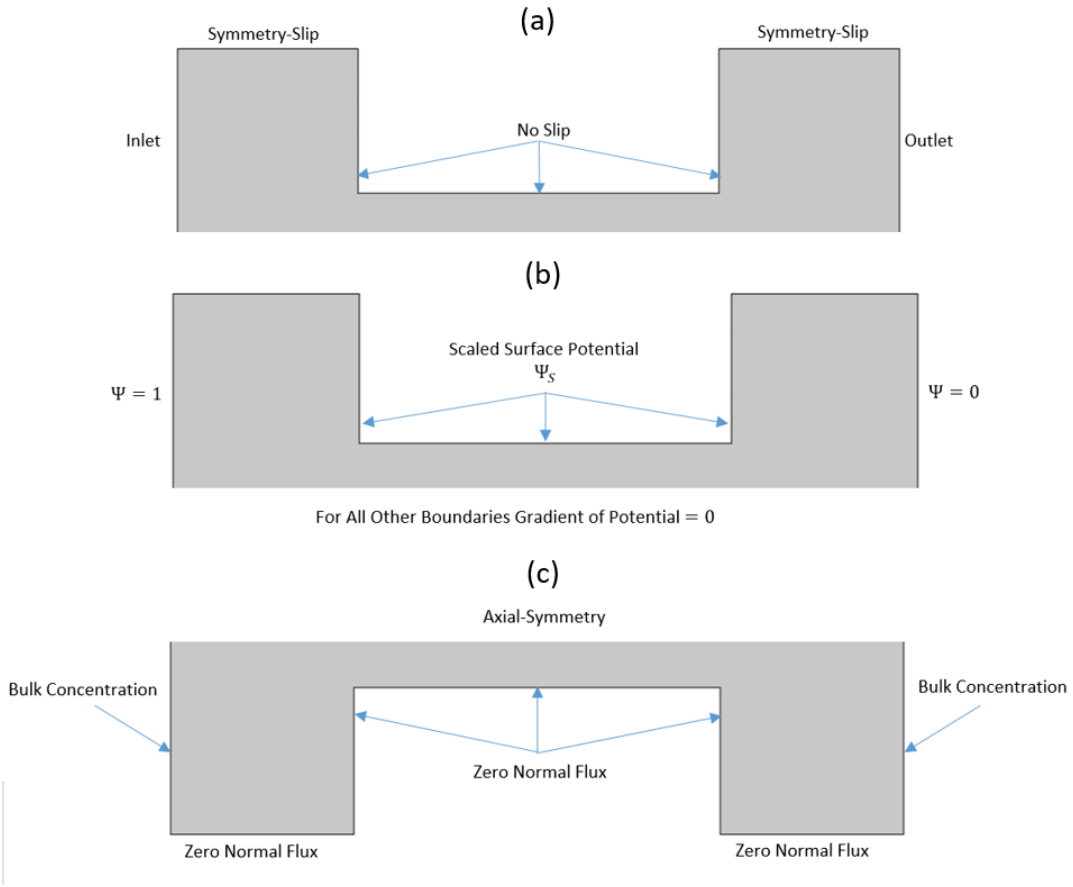

Figure 3.4 Boundary conditions for (a) momentum equation (b) Poisson equation and (c) Nernst–Plank equations for electroosmosis.

3.3 Numerical methodology and validation

3.3.1 **Numerical methodology**

The governing non-linear partial differential equations were solved using a commercial fully coupled finite element solver of COMSOL Multiphysics (V 5.3) [60]. The numerical methodology involves a segregated numerical method in which both the steady-state solutions for the Poisson and Nernst–Plank equations are first obtained for the no-flow case to get the quiescent electric

potential and ionic distributions. After which these distributions were used as the initial values for the fluid flow equations in order to solve for the velocity domain. From that initial point until the steady-state condition is reached, all the five governing equations, Eqs. (3.8—3.12), were solved together in a coupled manner in order to capture changes in ionic currents and the generated magnetic field until the steady-state solution is reached.

The generated mesh consists of two domains, as shown in Figure 3.5. All the five governing equations are solved together in the electrolyte domain, highlighted in Figure 3.5 (a), while only the Ampere-Maxwell equation is considered for the air domain shown in Figure 3.5 (b). At least 20,000 elements are needed to reach mesh independence. The simulations were conducted using 38,221 elements on a personal computer with a 4 core 3.4GHz processor and 32 GB RAM, highlighting the efficiency of the chosen computational domain. Quadratic triangular elements were used with a mesh refinement implemented near the upper wall; this is the region where the largest gradient in the electrical current and magnetic field is expected, and thus the results depend highly on the number of elements near the upper wall.

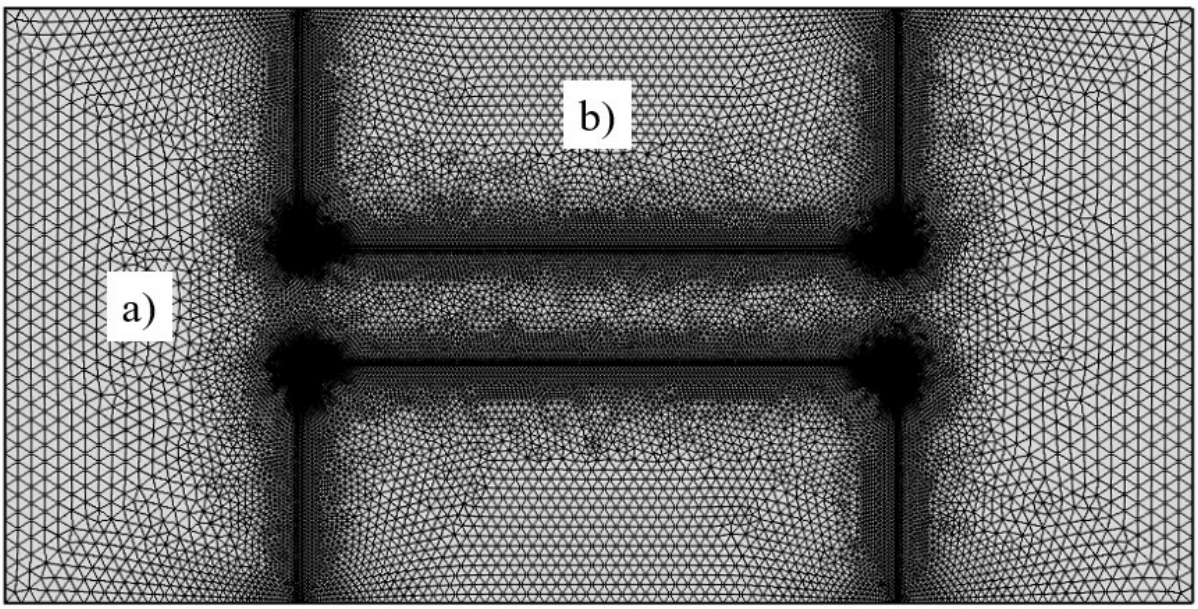

Figure 3.5 Meshed elements showing concentrated locations of the mesh showing (a) fluid domain (b) air domain

3.3.2 **Validation**

In this section, a detailed steady-state analytical model is presented. The analytical model is used to predict the evolution of streaming potential and development of an electrokinetic velocity profile as opposed to that of a typical shear driven flow problem due to electric double layer effects. The analytical model predicts the flow reversal phenomenon observed for high surface potentials, which will be discussed thoroughly in this section. The analytical results were validated using a transient numerical model that is also capable of determining the reformed velocity profile and the induced streaming potential. The results obtained for both models were compared to one another and all the simplifying assumptions used in the analytical model were tested against the numerical model.

3.4 Results and discussion

3.4.1 Analytical model for purely Electroosmotic flows

The analytical model and derivation for pure electroosmotic flow are presented in this section. The analytical model assumes a symmetric electrolyte solution transported by electroosmosis in a nanocapillary channel of infinite length with a surface potential on the walls of the capillary. The model only ignores axial concentration gradients and therefore neglects any entrance/exit effects. Here we summarize the key steps of the pertinent derivation.

The Poisson equation, Eq. (3.13), relates the electric potential distribution, Φ, with the free charge density, ρ_f, where ϵ is the dielectric permittivity of the bulk liquid.

$$\epsilon \nabla^2 \Phi = -\rho_f \tag{3.13}$$

Here, the electric potential (Φ) at a location (x, r) is considered to be the sum of the potential due to surface charge of the wall, or simply due to the electric double layer near the charged surface ($\psi(r)$) and the potential developed due to electroosmotic effects (xE_x). This superposition assumption is only valid if the variation in electric potential in the transverse direction is much bigger than the variation in the axial direction. This is a realistic assumption for nano/microchannels with very large aspect ratios ($L \gg a$), where L and a are the channel length and radius, respectively.

$$\Phi(r,x) \equiv \psi(r) + \emptyset_0 - xE_x \tag{3.14}$$

The free charge density is defined as $\rho_f = \sum z_i e n_i$, where z is the valence, e is the elementary charge and n_i is the ionic number concentration of the i^{th} ion in the solution. The movement of the ionic species in the solution is governed by the Nernst-Plank equation, which at a steady-state

is given by Eq.(3.15) where D_i is the diffusion coefficient of the i^{th} species, k_B is the Boltzmann constant and T is the absolute temperature.

$$\nabla.\left[n_i\boldsymbol{u} - D_i\nabla n_i - \frac{z_i e n_i D_i}{k_B T}\nabla\Phi\right] = 0 \tag{3.15}$$

Applying Eq. (3.15) in the r direction, where $u_r = 0$, results in the Boltzmann distribution for the ionic species, $n_i = n_{i_\infty} exp\big(-z_i e/K_B T\,\psi(r)\big)$, with n_∞ being the bulk ionic concentration. Therefore, the free charge density can be expressed as:

$$\rho_f = e(z_+ n_+ + z_- n_-) \tag{3.16}$$

$$\rho_f = ezn_\infty(-2\sinh(z_i e\psi/K_B T) \tag{3.17}$$

Introducing the expression for the electric potential and ionic distribution, given in Poisson's equation, gives the nonlinear Poisson-Boltzmann equation as:

$$\frac{1}{r}\frac{\partial}{\partial r}(r\frac{\partial\psi}{\partial r}) = k^2 sinh\left(\frac{ze}{K_B T}\psi(r)\right) \tag{3.18}$$

In which the Debye length is defined as $k^{-1} = \left(\frac{\epsilon K_B T}{2e^2 z^2 n_\infty}\right)^{1/2}$.

The boundary conditions for Eq. (3.16) are $\psi = \xi$ at $r = a$ and $d\psi/dr = 0$ at $r = 0$. The solution to this equation is:

$$\psi(r) = \zeta\,\frac{I_0(\kappa r)}{I_0(\kappa a)} \tag{3.19}$$

Here κ is the inverse double layer thickness, $\kappa = (2z^2 e^2 n_\infty/\epsilon K_B T)^{1/2}$ and I_0 is the first kind modified Bessel function.

3.4.1.1 Flow velocity

The flow field is governed by the modified Naiver-Stokes equation including the electrical body force as shown in Eq. (3.20). Naiver-Stokes equations were implemented assuming stokes flow with negligible inertial and turbulence effects.

$$0 = \mu \frac{1}{r}\frac{\partial}{\partial r}\left(r\frac{\partial u_x}{\partial r}\right) + \rho_f E_x \tag{3.20}$$

Where μ is the dynamic viscosity of the electrolyte solution, u_x is the axial velocity, ρ_f is the free charge density within the liquid and E_x is the applied electric field in the x-direction.

In order to derive an equation for the velocity profile, Poisson-Boltzmann and Nernst-plank equations are needed to capture the fluid flow due to electroosmosis. Making use of Poisson's equation ($\epsilon\nabla^2\Phi = -\rho_f$) along with Solving Eq. (3.20) with boundary conditions: $r = 0$, $\frac{\partial u_x}{\partial r} = 0$ and $r = -\mathrm{a}\,, u_x = 0$ results in the following:

$$u(r) = -\frac{\epsilon\xi}{\mu}\left[1 - \frac{I_0(\kappa r)}{I_0(\kappa a)}\right]E_x \tag{3.21}$$

Eq. (3.21) presents that velocity profile due to purely electroosmotic flow. The velocity is maximum at the center of the channel and its magnitude is directly proportional to the applied electric field, the electric permittivity of the electrolyte solution and the zeta potential of the capillary wall. The velocity is also opposite to the direction of the applied electric field and inversely proportional to the viscosity of the fluid.

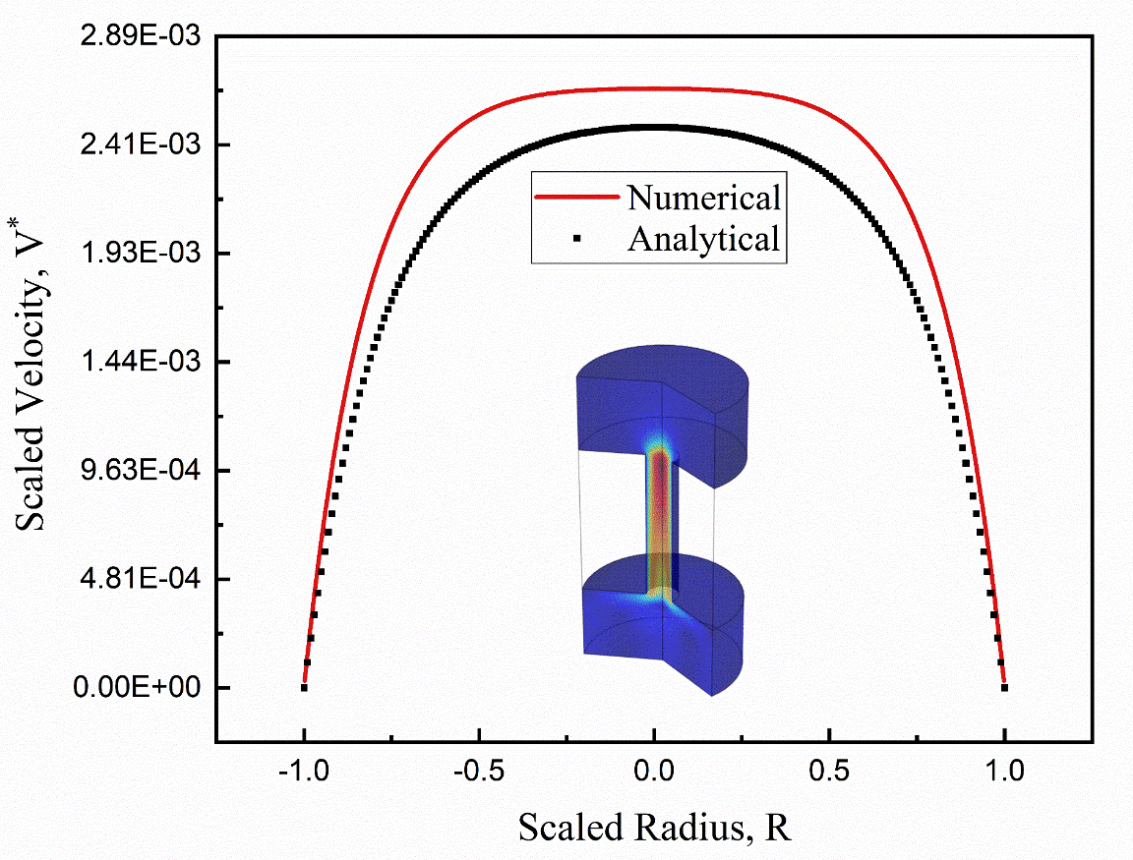

Figure 3.6 Shows Plot showing scaled velocity at the midplane of the nanochannel versus scaled radius for purely electroosmotic flow case. $\kappa a = 5$.

Figure 3.6 shows good agreement between the numerical and analytical results of the velocity distribution. The numerical results show that scaled electroosmotic velocity is maximum and has a plug-like velocity near the center. This plug-like velocity can be attributed to the fact that the free ion density is almost zero near the center of the channel. Therefore, the electrokinetic force applied to the electrolyte molecules near the center is significantly weak, creating no shearing effects i.e., zero velocity gradients. The analytical results show slightly lower values than the numerical results, mainly due to the simplifying assumption of having a one-dimensional flow that

was implemented in the analytical model [13]. Plots of the pressure distribution can be found in the Appendix.

3.4.1.2 Electrical current

The total current flow per unit length of the channel can be expressed as:

$$I = 2\pi \int_0^a i_x \, r \, dr \tag{3.22}$$

Where the current density in the x-direction is given by:

$$i_x = eu\sum z_i n_i - e\sum D_i z_i \frac{dn_i}{dx} + \frac{e^2}{K_B T} E_x \sum z_i^2 D_i n_i \tag{3.23}$$

In our analytical derivation, we assumed that there is no ion concentration gradient in the axial direction ($\partial \mathrm{n_i}/\partial \mathrm{x} = 0$). Therefore, the total current consists of only two terms. The first term in the expression of the total current is referred to as the streaming current and is caused by the convective transport of the excess ions in the mobile double layer region (diffuse layer) near the charged interface, where the electroneutrality term $\sum z_i n_i$ is not zero. The second term, referred to as the conduction current, is due to electric conduction through the liquid along the channel.

Assuming the same diffusion coefficient ($D_+ = D_- = D$) and bulk concentration ($n_{+\infty} = n_{-\infty} = n_\infty$) for the positive and negative ions, the conduction current can be written as:

$$I_C = 4\pi \frac{z^2 e^2 D}{K_B T} n_\infty E_x \int_0^a \cosh\left(\frac{ze}{K_B T}\psi(r)\right) r \, dr \tag{3.24}$$

Considering the electric conductivity σ^∞ as:

$$\sigma^\infty = 2\frac{z^2 e^2 D}{K_B T} n_\infty \tag{3.25}$$

We find that substituting Eq. (3.18) into Eq. (3.23) can be further simplified into:

$$I_C = \sigma_\infty E_x H\, F_{cs} \tag{3.26}$$

In the above expression, F_{cs} is a parameter that shows the non-electroneutrality of the solution ($\sum z_i^2 n_i \neq 0$) due to the formation of the electrical double layer near the charged wall. The electrolyte solution's conductivity can be considered to have changed due to the formation of an electric double layer where the new conductivity is defined by $\sigma_{FluidwithEDL} = \sigma_\infty F_{cs}$.

$$F_{Cs} = 1 + \left(\frac{ze\xi}{K_B T}\right)^2 \frac{1}{I_0^2(\kappa a)} \int_0^1 I_0^2(\kappa a\ .\ R)\ R\ dR \tag{3.27}$$

The streaming current can be written as:

$$I_S = \int_0^a u\left(-\epsilon \frac{d^2\psi(r)}{dr^2}\right) dr \tag{3.28}$$

3.4.1.3 Magnetic field

In order to find an analytical expression for the magnetic fields, we applied Ampere's law for a closed circular loop of radius "r" around the nanochannel. The magnetic field must have a constant magnitude around the loop due to the symmetric nature of the problem, as shown by Eq. (3.29)

$$\oint \boldsymbol{B}\ .\ dl = \mu_0 \mathrm{I}_{\mathrm{total}},; B = \frac{\mu_0 \mathrm{I}_{\mathrm{total}}}{2\pi r}, r > a \tag{3.29}$$

It is clear from Eq. (29) that the magnetic flux density decreases as we move further away from the nanochannel. However, the behavior of the magnetic flux density inside the nanochannel is more difficult to predict. This is mainly because of the non-uniformity of the current profiles within the nanochannel caused by non-uniform streaming current profiles. Here we show the analytical

approach to generate internal magnetic fields. In order to find the magnetic field inside the nanopore, we need to integrate the non-uniform streaming current density for r < R, as shown here:

$$\oint \boldsymbol{B} \,.\, dl = \mu_0 \mathrm{I}_{\mathrm{enclosed}}, ; B = \frac{\mu_0 \mathrm{I}_{\mathrm{enclosed}}}{2\pi r}, r < a \tag{3.30}$$

$$\mathrm{I}_{\mathrm{enclosed}} = 4\pi \frac{z^2 e^2 D}{K_B T} n_\infty E_x \int_0^r \cosh\left(\frac{ze}{K_B T}\psi(r)\right) r \, dr + \int_0^r u\left(-\epsilon \frac{d^2\psi(r)}{dr^2}\right) dr \tag{3.31}$$

It is important to note that these analytical expressions do not take into account the transient effects and can only be used to validate the steady-state magnetic flux density. Also, the expression is based on an assumption of an infinite nanochannel length, and thus the results are only a function of radius. Therefore, these results can only be compared to the 2-D numerical results at the mid-length of the nanochannel. Similarly, analytical expressions can be obtained for the shear-driven streaming potential using Ampere's law and the ionic current expressions defined in Chapter 2 of our work.

$$\oint \boldsymbol{B} \,.\, dl = \int \mu_0 \, J_{total} \, dA \, ; B = \mu_0 J_{\mathrm{total}}(H), y > H \, ; B = -\mu_0 J_{\mathrm{total}}(H), y < H \tag{3.32}$$

It is clear from these expressions that the magnetic flux density is almost constant outside of the nanoslit, which makes it ideal for non-invasive sensing of biomolecules. Also, due to the non-symmetric nature of this case, the magnetic field inside the nanoslit is predicted to vary nonlinearly.

3.4.2 **Comparison of numerical and analytical results**

The results highlighted in this section are divided into two areas. In the first part, we interpret the electrokinetic aspects of the flow, mainly the ionic current distribution, for both streaming potential

and electroosmotic flows. This sets the stage for analyzing the magnetic fields generated due to these ionic currents that flow within the nanochannels. The second part is focused on analyzing the magnetic field distribution generated inside and outside of the nanochannels. These analyses are beneficial to determine the effect of the magnetic field on the transport path of any biomolecules with induced dipoles; they can be used as a secondary electromagnetic signal as part of a sequencing technique. As mentioned previously, shear driven streaming potential flows have two modes of operation. Results for both the streaming potential mode (no net current between the reservoirs) and the streaming current mode (no net electrical potential between the reservoirs) are presented in this section.

3.4.2.1 Electrical currents

The steady-state electrical current distributions for both the shear driven streaming potential flow and electroosmotic flow are plotted. The ionic current density was obtained for our simulation at the midplane of the nanochannel and therefore avoiding any entrance or exit effects. These numerical results were compared against the analytical expressions presented in the previous section in order to determine the validity of our simplifying assumptions.

The electrokinetic flow of electrolytes in nanochannels with charged walls induces streaming currents inside the nanochannel. The fluid flow creates a tangential force applied on the hydrodynamically mobile part (diffuse layer) of the electrical double layer, which transports the free ions along the flow direction. This ionic convective flux is labeled as the streaming current. The streaming current phenomenon has been extensively employed in surface characterization devices, mainly for estimating zeta-potentials. However, accurate measurement of these currents has been significantly challenging. Figure 3.7 shows the current density distribution for the shear driven streaming potential flow. The numerical and analytical results for both streaming and total

current densities are in good agreement; however, there is a discrepancy in the conduction current density near the moving wall. The streaming current density has its peak value ($2.9\ A/m^2$) near the moving charged wall and then decays to zero, as it is mainly dependent on the Debye length and flow velocity as shown in Eq. (3.28). Moreover, the streaming current density is mostly in the same direction as the flow, while the conduction current is in the opposing direction as predicted by our analytical model. However, the analytical model shows the conduction current density is higher than the numerical model, near the moving wall. In order to determine the reason for this, the electric field distribution must be analyzed. It is important to note that the analytical model assumes that the induced electric field is constant along the width of the channel. However, the numerical model shows that the electric field is not constant throughout the channel width and decays to zero near the moving charged wall. This, in turn, affects the conduction current density distribution as it mainly depends on the electric field and free charge density as shown in Eq. (3.26). Therefore, we can conclude that the assumption of a constant electric field is not valid. Figure 3.8 shows the current density distribution for the streaming current flow case using the same exact conditions stated for Figure 3.7. The only difference between these two cases is that the streaming potential mode has a zero overall current while in the streaming current mode, a net current exists based on the electrical connection. Figure 3.8 shows that the total current density is always in the positive direction, suggesting the presence of net total current. The streaming current density has its peak value ($2.3\ A/m^2$) in the vicinity of the wall while the conduction current density is nearly zero along the entire channel width. It should also be noted that the maximum induced electric field is much lower for the streaming current case ($600\ V/m$) than that of the streaming potential case ($2750\ V/m$). This consequently significantly decreases the generated conduction current density for the streaming potential mode. Figure 3.9 shows the electrical current

density distribution for electroosmotic flow in a nanocapillary. Streaming current density is directly proportional to the free charge density and the flow velocity. Figure 3.6 shows that velocity is maximum at the center and has a plug-like shape that decays to zero at the capillary walls while the free charge density is maximum near the charged walls. This combined effect causes the streaming current to reach its peak value ($0.021\ A/m^2$) at a location between the center and the walls of the capillary, depending on the Debye length. Furthermore, Conduction currents are significantly dominant over streaming currents in electroosmotic flows, while streaming currents dominate for streaming potential flows as presented by Figure 3.7 and Figure 3.9.

Moreover, the numerical and analytical results for streaming current density are in good agreement, while there are discrepancies for both the conduction and total current densities, particularly near the charged walls. The reason behind this disagreement is again in the assumption of zero electric field variation along the radial direction. It is clear from our simulation results that the electric field is zero near the capillary walls; this results in a zero conduction current near the wall. The analytical model, on the other hand, assumes an average constant electric field that leads to the prediction of a peak conduction current near the walls. This assumption is physically unattainable, as having an ionic flux at the wall of the capillary essentially breaks down the no-slip condition for the walls.

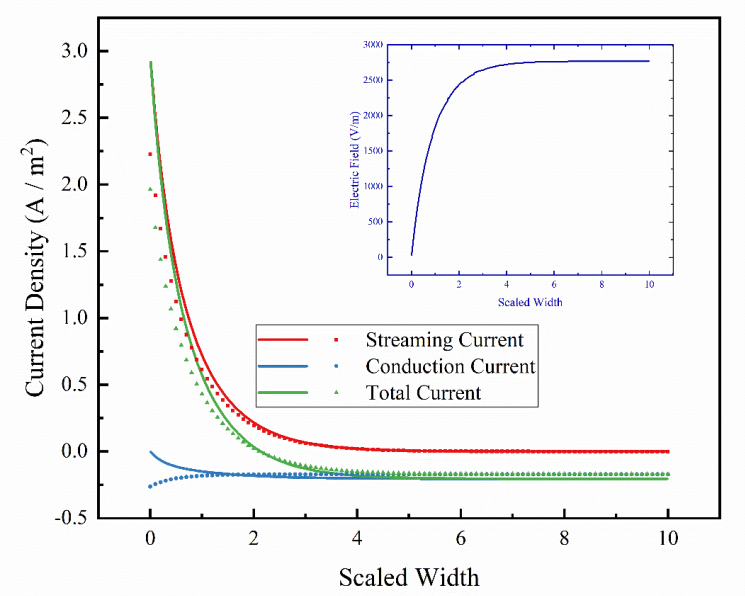

Figure 3.7 Plot showing numerical (solid lines) vs analytical (dashed line) solution for streaming, conduction, and total current distribution for shear driven streaming potential flows (streaming potential mode). The inset plot shows the electric field distribution along the non-dimensional height of the microchannel. $\kappa H = 10$ $\psi_S = 1$.

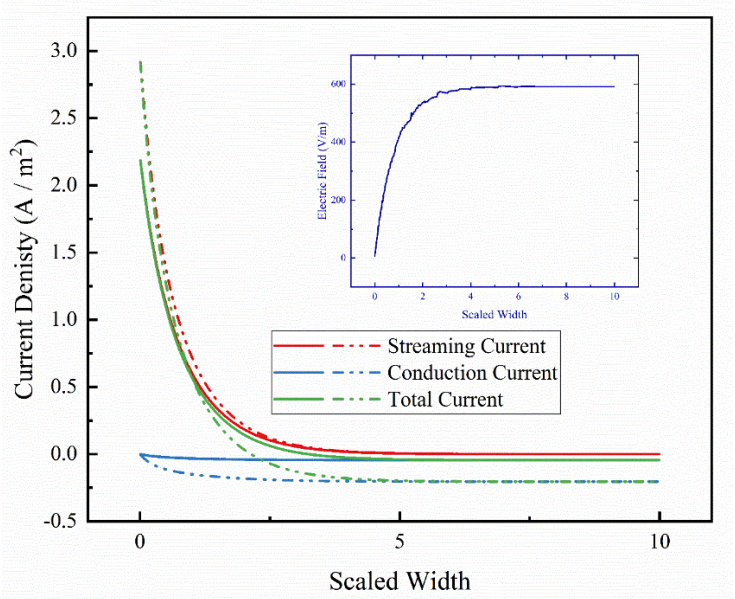

Figure 3.8 Plot showing numerical (solid lines) vs analytical (dashed line) solution for streaming, conduction, and total current distribution for shear driven streaming potential flows (streaming current mode). The inset plot shows the electric field distribution along the non-dimensional height of the microchannel. $\kappa H = 10$ $\psi_S = 1$.

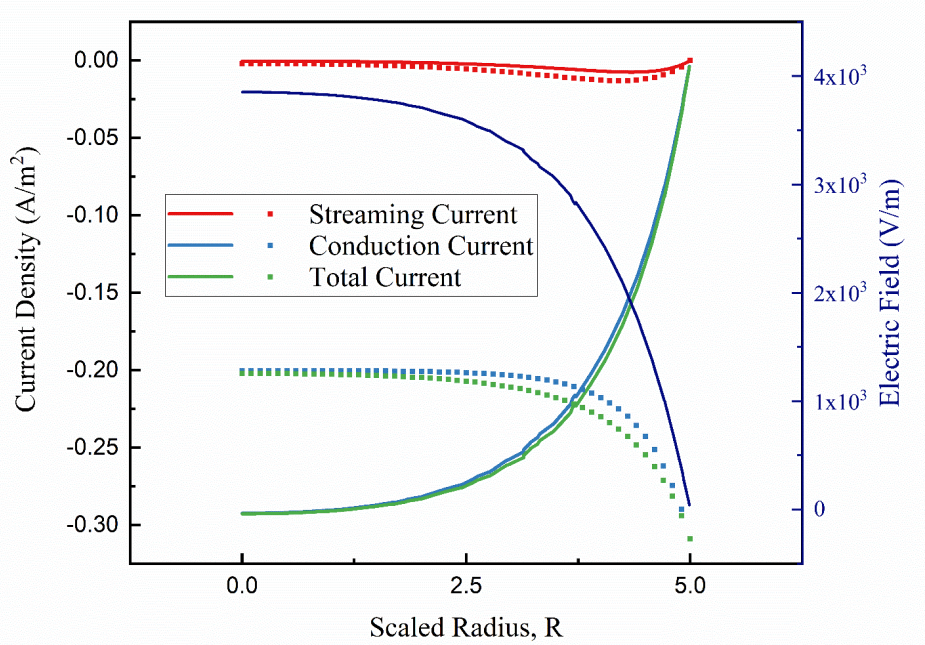

Figure 3.9 Plot showing numerical (solid lines) vs analytical (dashed line) solution for streaming, conduction and total current distribution for electroosmotic flows. The blue plot shows the electric field distribution along the non-dimensional height of the microchannel. $\kappa a = 5$ $\psi_S = 1$.

3.4.2.2 Magnetic field

In the previous section, we discussed and analyzed different aspects of electrokinetic flows and ionic currents in nanochannels for both streaming potential and electroosmotic flows. In this section, the magnetic fields induced by the different current fluxes for both electroosmosis and streaming potential are investigated. The results presented in this section were obtained using the same simulation parameters that were used to evaluate the ionic current densities.

Figure 3.10 shows the magnetic flux density distribution inside and outside of the nanochannel for electroosmotic flow. The vertical line at a scaled radius, $R = 5$, represents the outer surface of the nanocapillary. The most significant qualitative observations are that, in the mid-length of the channel, the magnetic flux density is only a function of the radial coordinate, the peak value of the magnetic field is in vicinity of the charged walls of the nanocapillary, and extends outside of it where it can be possibly measured by a micro-electromagnetic sensor [77]. The reason behind the

magnetic flux reaching its maximum near the nanocapillary walls is due to the total current that flows within the channel. The total current is simply the integral of the total current density presented in Figure 3.9. Figure 3.9 shows that the total current density inside the nanocapillary is never zero and therefore the total current continues to increase until the outer radius is reached, where the magnetic flux density reaches its maximum of 680 fT. It should also be noted that this peak value eventually decays to zero at the centerline of the nanocapillary due symmetry and in the far-field as we move further away from the nanocapillary. It is also worth comparing the magnitude of our numerical results with the analytical results of the idealized case of an infinitely long capillary. Figure 3.10 shows excellent agreement between the numerical and analytical results for the magnetic flux density. This level of agreement can be attributed to making the comparison at the mid-length of a relatively long nanocapillary.

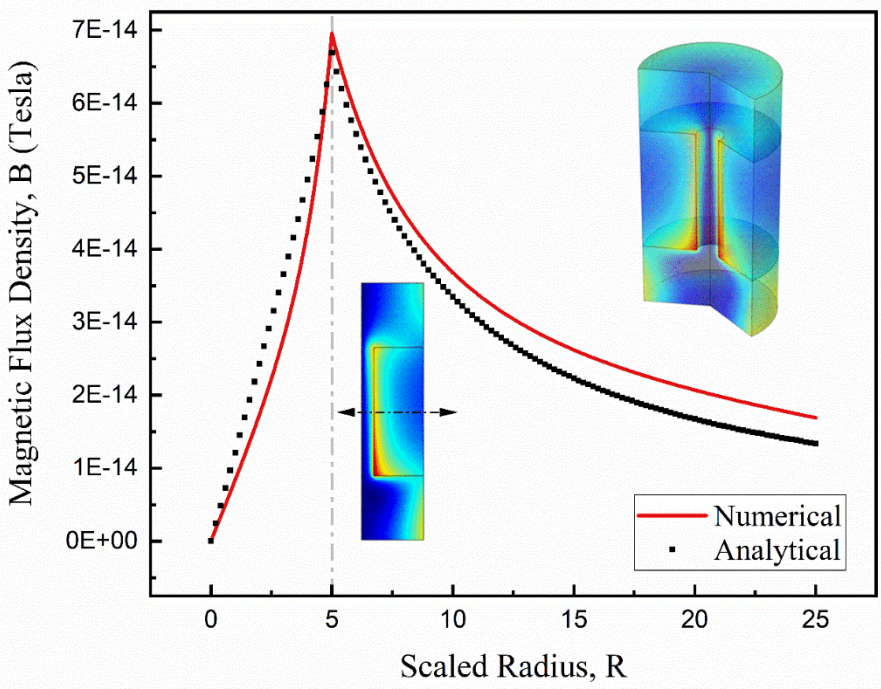

Figure 3.10 Plot showing numerical (solid lines) vs. analytical (dashed line) solution for the magnetic flux density distribution for electroosmotic flows at the mid-plane of the microchannel. The vertical line at R=1 represents the outer surface of the microchannel. $\kappa a = 5$ $\psi_s = 1$.

Figure 3.11 and Figure 3.12 present the internal and external magnetic flux density distribution for streaming potential and streaming current flow, respectively. Both figures show that the magnetic flux density is zero inside the nanochannel near the moving charged wall. This is mainly attributed to the non-symmetry of the flow leading to a non-uniform current density distribution as highlighted by Figure 3.7 and Figure 3.8. The total current is higher near the walls for the streaming potential mode ($2.9\ A\backslash m^2$) than for the streaming current mode ($2.3\ A\backslash m^2$). This leads to the location of the zero magnetic flux density shifting slightly upwards from the streaming current mode (27.47) to the streaming potential mode (27.55). Based on our simulations, the external magnetic flux density is constant, except in the area close to the inlet and outlet of the nanochannel. The constant value does not depend on the distance from the channel. Also, it is noted that the maximum value of the magnetic flux density is in the vicinity of the upper charged wall and extends outside of the nanochannel where it can potentially be recorded. The maximum value for the streaming current mode (52.9 fT) is higher than for the streaming potential mode (50.3 fT).

Now that we predicted the presence of both internal and external magnetic fields in nanochannels, two possible applications for biomolecules with an induced dipole are envisioned. The first application is the use of these external magnetic field readouts as a non-invasive electronic signature for biomolecules. This can help with enhancing the current RNA/ DNA sequencing techniques. Magnetic fields, as small as Femto Tesla, which is in the same range as our simulation results, are detectable and measurable for both electroosmotic and shear-driven streaming potential flows in nanochannels[77–79]. An important advantage for using shear driven slit microchannels over electroosmotic flows in nano-capillaries is that the external magnetic field is constant and thus can be detected more precisely. The second application is in using the internal magnetic field as a method to segregate and manage the transport of biomolecules. A biomolecule with an induced

dipole entering the nanochannel will be subjected to an electromagnetic radial force that can cause the biomolecule to be displaced to specified radial locations and move along with the local axial flow velocity. These proposed applications are supported by experimental findings in the field of medicine and biology. [77–79].

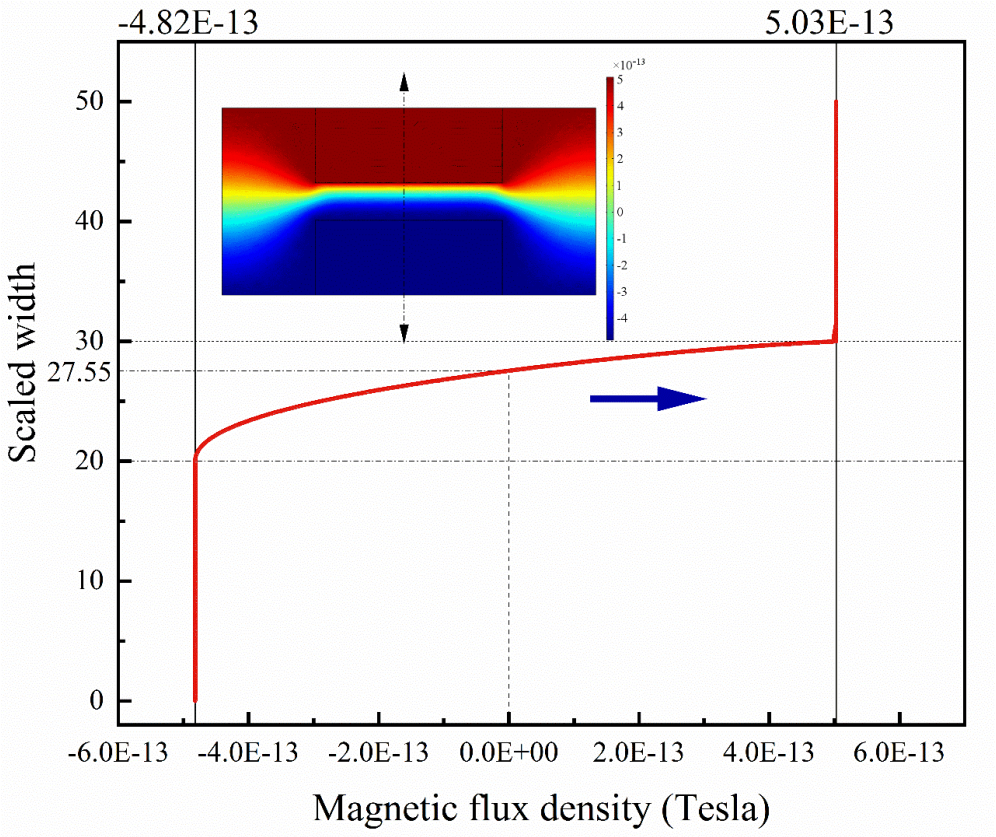

Figure 3.11 Plot showing numerical for the magnetic flux density distribution for streaming potential flows in microchannels (streaming potential case). The blue arrow shows the direction of fluid flow. $\kappa H = 10$ $\psi_S = 1$.

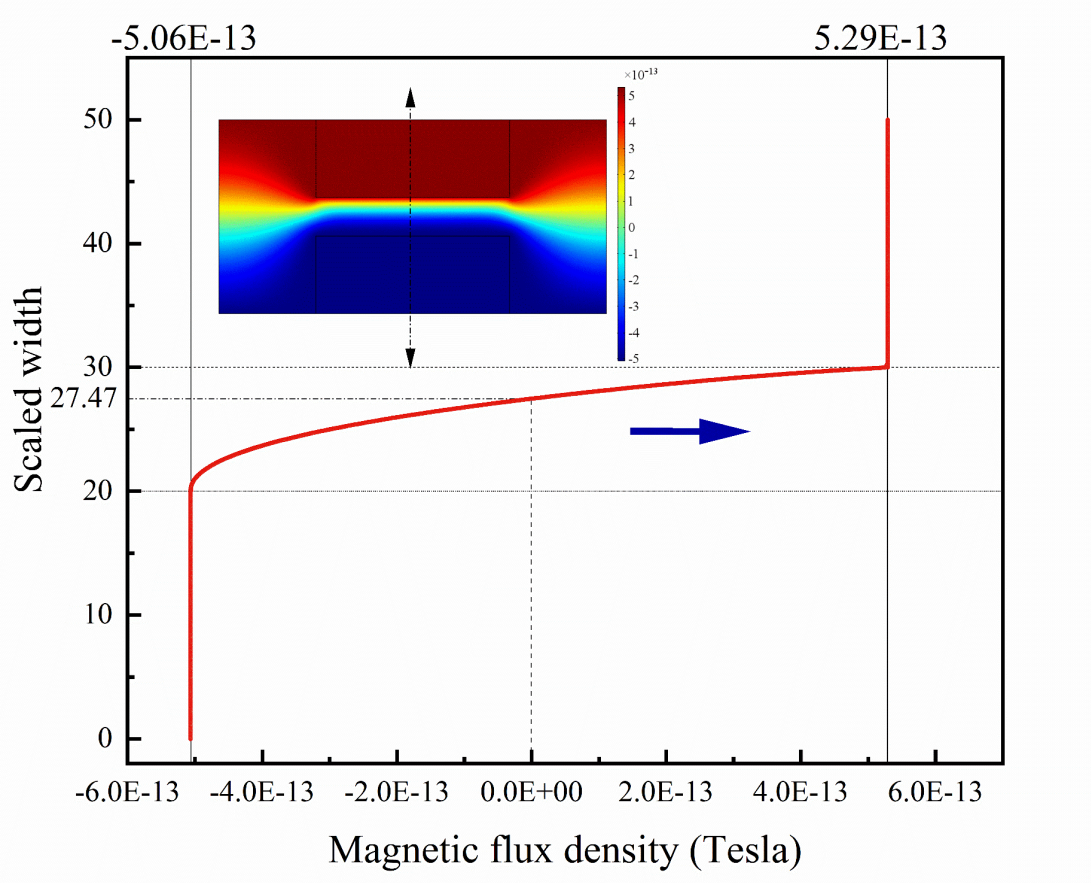

Figure 3.12 Plot showing numerical solution for the magnetic flux density distribution for streaming potential flows in microchannels (streaming current case). The blue arrow shows the direction of fluid flow. $\kappa H = 10\ \psi_S = 1$.

3.4.3 **Development of electrokinetic effects: transient analysis**

3.4.3.1 Transient analysis of currents for streaming potential flows

Figure 3.13 shows the average current density versus scaled time for streaming potential shear driven flows for both the streaming potential mode and the streaming current mode. As expected, the streaming current mode has a larger average current density ($0.132\ A/m^2$) than the streaming potential mode ($0.022\ A/m^2$). This is because of the electrical connection employed between the two reservoirs in the streaming current mode that prevents charge buildup and induced streaming

potential. However, in the streaming potential mode charges accumulate downstream, setting up an electrical field which in turn acts on the charges in the fluid impacting the overall current distribution. This trans-capillary electric field, created by the imbalance of charges near the entrance and exit, generates a conduction current in the direction opposite to the streaming current that travels through any electrical path available. At steady state, the conduction current cancels out the convective ionic flux. Our numerical simulation, however, shows that at steady state there will be a small net current in the streaming potential mode that might be indetectable.

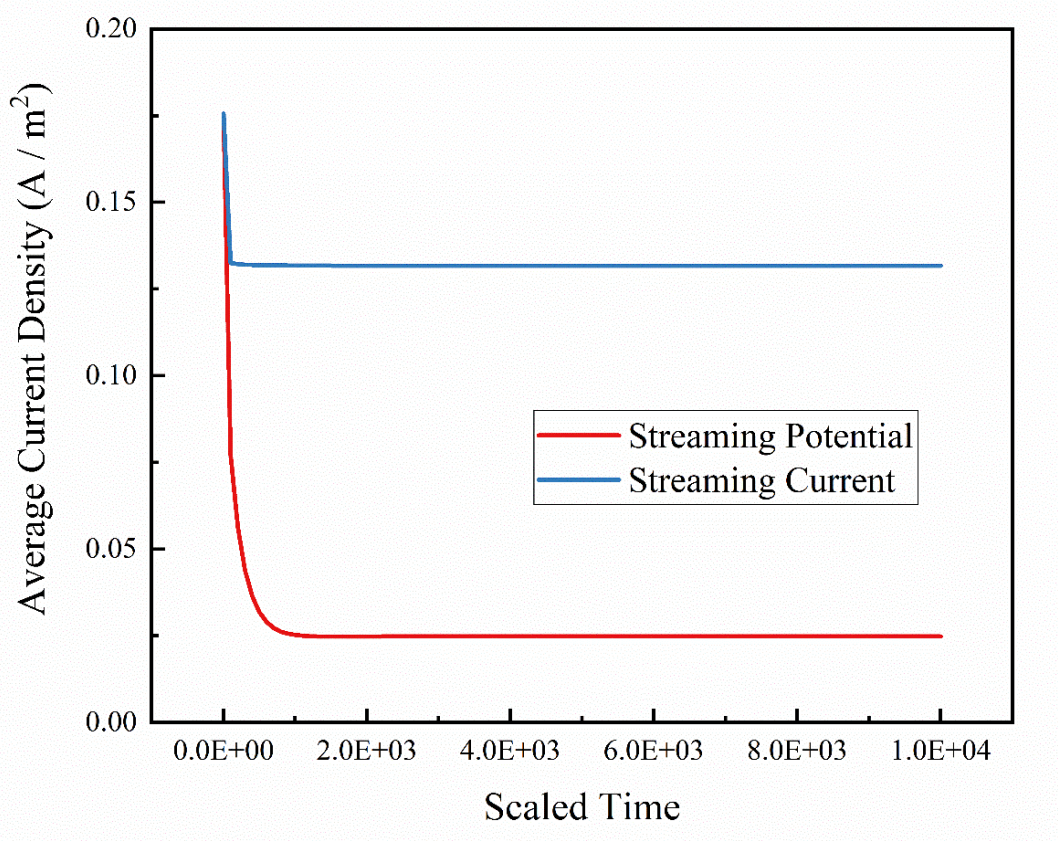

Figure 3.13 Plot showing the average total current density over time for streaming potential and streaming current flows in microchannels. $\kappa H = 10$ $\psi_S = 1$.

3.5 Concluding Remarks

In this paper, a numerical model validated by analytical expressions was proposed to model the internal and external magnetic field generated by the ionic current in electrokinetic flows in nanochannels. The proposed model involves solving a set of Poisson, Nernst-Planck, Ampere-Maxwell's and Navier-Stokes governing equations to simulate the generated internal and external magnetic field in electrokinetic flows. The results show that the magnetic fields outside shear driven slit microchannels remain constant, making it suitable for taking reliable non-invasive external magnetic fields' readouts. These readouts can be employed in various applications to determine the zeta potential of surfaces or to perform DNA sensing and sequencing. The results also show that maximum magnetic field readouts for electroosmotic flows takes place at the surface of the nanochannel and then decays rapidly outside of the nanochannel.

Moreover, other features concerning the ionic currents in electrokinetic flows were examined. The results highlight some problems with the constant electric field assumption employed for most analytical models used in the literature. It also examines the transient effects of the generated ionic currents. Finally, our analysis provides a detailed understanding of the characteristics of the magnetic field and ionic currents generated by electroosmotic and streaming potential flows. The model proves the existence of detectable levels of magnetic fields in electrokinetic flows.

4 Conclusion and Future Work

4.1 Conclusion

Lab-on-chip devices have gotten increasing attention for their promising applications in fields like DNA analysis and other biomedical applications. A lot of research has been conducted to further understand that flow behavior in microchannels in lab-on-chip devices. The physics of the fluid motion involved in microchannels is a subdiscipline of fluid dynamics, with adjustments made based on the smaller size of microchannels. The field of electrokinetics, involved in the motion of fluids, overarches two important phenomena that are discussed in this thesis: streaming potential flow and electroosmotic flow. The first chapter of the thesis discussed flow reversal in shear driven streaming potential flows. Based on the numerical model that was developed and the analytical expressions that were derived from the governing set of equations, results showed that the analytical expressions were able to fully support the validity of the numerical expressions. The results show that the interfacial charge of the moving interface greatly impacts the velocity profile of the flow and can reverse its overall direction. Both the numerical model and the analytical expressions anticipated the occurrence of the flow reversal phenomena in shear driven streaming potential flows at a surface potential above 120mV between the fluid-liquid interface of the oil and water system.

The second chapter focused on the magnetic fields induced by the flow of electric charges through the microchannels, both in the case of electroosmotic flows and streaming potential flows. The effects of ionic currents on the induced magnetic field both inside and outside of the microchannels were modeled and compared with known analytical solutions. The results also show that the maximum magnetic flux density readout for electroosmotic flows takes place at the surface of the nanochannel and then decreases exponentially outside of the nanochannel. Moreover, other features concerning the ionic currents in electrokinetic flows were examined. The results highlight

some issues with the constant electric field assumption employed for most analytical models used in the literature. Finally, the obtained results proposed that the notion of using the magnetic field detected outside of the nanochannels as a secondary electromagnetic signal for biomolecules as a part of a DNA sequencing technique.

4.2 Future works

The future direction of research can be investigating the rheological effects of the electrolytes used in electrokinetic flows, modeling a network of nanopores, and an electrokinetic power conversion system as follows:

1- Simulating a network of nanopores connected between two reservoirs to model electrokinetic transport in porous media where there is a heterogeneity in the porous microstructure. This can help to analyze the ion rejection mechanism in membranes' porous network.

2- Most of the electrolytes employed in lab-on-chip and microfluidic devices are of non-Newtonian nature. Implementing a power-law model for dilatant and pseudo-plastic fluids is worth investigating.

3- Investigating the use of electrokinetic flow microchannels as a way of harvesting energy for nano-sized applications.

References

[1] N.T. Nguyen, S.A.M. Shaegh, N. Kashaninejad, D.T. Phan, Design, fabrication and characterization of drug delivery systems based on lab-on-a-chip technology, Adv. Drug Deliv. Rev. 65 (2013) 1403–1419. doi:10.1016/j.addr.2013.05.008.

[2] A.M. Streets, Y. Huang, Chip in a lab: Microfluidics for next generation life science research, Biomicrofluidics. (2013). doi:10.1063/1.4789751.

[3] F. Bragheri, R.M. Vazquez, R. Osellame, Chapter 12.3 - Microfluidics, in: Three-Dimensional Microfabr. Using Two-Phot. Polym., Elsevier Inc., 2016: pp. 310–334. doi:10.1016/B978-0-323-35321-2/00016-9.

[4] G.T. Vladisavljević, N. Khalid, M.A. Neves, T. Kuroiwa, M. Nakajima, K. Uemura, S. Ichikawa, I. Kobayashi, Industrial lab-on-a-chip: Design, applications and scale-up for drug discovery and delivery, Adv. Drug Deliv. Rev. 65 (2013) 1626–1663. doi:10.1016/j.addr.2013.07.017.

[5] P.C. Gach, K. Iwai, P.W. Kim, N.J. Hillson, A.K. Singh, Droplet microfluidics for synthetic biology, Lab Chip. 17 (2017) 3388–3400. doi:10.1039/c7lc00576h.

[6] G.M. Whitesides, The origins and the future of microfluidics, Nature. 442 (2006) 368–373. doi:10.1038/nature05058.

[7] A. Mansouri, C. Scheuerman, S. Bhattacharjee, D.Y. Kwok, L.W. Kostiuk, Transient streaming potential in a finite length microchannel, J. Colloid Interface Sci. (2005). doi:10.1016/j.jcis.2005.05.094.

[8] B.E. Rapp, Introduction, in: Microfluid. Model. Mech. Math., 2017: pp. 3–7. doi:10.1016/b978-1-4557-3141-1.50001-0.

[9] S.J. Perkins, Protein volumes and hydration effects, Eur. J. Biochem. (1986). doi:10.1111/j.1432-1033.1986.tb09653.x.

[10] S.J. Park, M.K. Seo, Intermolecular Force, 2011. doi:10.1016/B978-0-12-375049-5.00001-3.

[11] K. Scott, Electrokinetic Separations, Handb. Ind. Membr. (1995) 793–800. doi:10.1016/b978-185617233-2/50022-2.

[12] J.H. Masliyah, S. Bhattacharjee, Electrokinetic and Colloid Transport Phenomena, John Wiley & Sons, New Jersey, USA, 2006.

[13] S. Bhattacharyya, Z. Zheng, A.T. Conlisk, Electro-osmotic flow in two-dimensional charged micro- and nanochannels, J. Fluid Mech. (2005). doi:10.1017/S0022112005005720.

[14] M. Methods, M.Z. Potential, Chapter 10 Microfluidic methods for measuring zeta potential, Interface Sci. Technol. 2 (2004) 617–640. doi:10.1016/S1573-4285(04)80032-2.

[15] C.J.F.P. Jones, J. Lamont-Black, S. Glendinning, Electrokinetic geosynthetics in hydraulic applications, Geotext. Geomembranes. 29 (2011) 381–390. doi:10.1016/j.geotexmem.2010.11.011.

[16] A.F. Ismail, K.C. Khulbe, T. Matsuura, RO Membrane Characterization, 2019. doi:10.1016/b978-0-12-811468-1.00003-7.

[17] H.A. Stone, A.D. Stroock, A. Ajdari, Engineering Flows in Small Devices, Annu. Rev.

Fluid Mech. 36 (2004) 381–411. doi:10.1146/annurev.fluid.36.050802.122124.

[18] S.F.Y. Li, Y.S. Wu, Capillary electrophoris, in: Encycl. Sep. Sci., 2000: pp. 1176–1187. doi:10.1021/ac00171a002.

[19] L. Karpenko-Jereb, T. Araki, Modeling of Polymer Electrolyte Fuel Cells, Elsevier Inc., 2018. doi:10.1016/b978-0-12-811459-9.00003-7.

[20] R.J. Yang, L.M. Fu, Y.C. Lin, Electroosmotic flow in microchannels, J. Colloid Interface Sci. 239 (2001) 98–105. doi:10.1006/jcis.2001.7551.

[21] H. Kamiya, Y. Otani, M. Fuji, M. Miyahara, Characteristics and Behavior of Nanoparticles and Its Dispersion Systems, 2018. doi:10.1016/B978-0-444-64110-6.00003-2.

[22] A. Asadi, B.B.K. Huat, H. Nahazanan, H.A. Keykhah, Theory of electroosmosis in soil, Int. J. Electrochem. Sci. 8 (2013) 1016–1025.

[23] H. Sasabe, Electrical properties, in: Colloid Interface Chem. Water Control, 1975: pp. 79–136. doi:10.2115/fiber.31.11_P360.

[24] A. Mansouri, P. Taheri, L.W. Kostiuk, Streaming current magnetic fields in a charged nanopore, Sci. Rep. (2016). doi:10.1038/srep36771.

[25] M.R. Sheffer, D.W. Oldenburg, Three-dimensional modelling of streaming potential, Geophys. J. Int. (2007). doi:10.1111/j.1365-246X.2007.03397.x.

[26] J.D. Sherwood, Streaming potential generated by two-phase flow in a capillary, Phys. Fluids. (2007). doi:10.1063/1.2717847.

[27] C. Kuang, F. Yang, W. Zhao, G. Wang, Study of the rise time in electroosmotic flow

within a microcapillary, Anal. Chem. (2009). doi:10.1021/ac901017a.

[28] C. Yang, C.B. Ng, V. Chan, Transient analysis of electroosmotic flow in a slit microchannel, J. Colloid Interface Sci. (2002). doi:10.1006/jcis.2002.8219.

[29] C.L. Rice, R. Whitehead, Electrokinetic flow in a narrow cylindrical capillary, J. Phys. Chem. 69 (1965) 4017–4024. doi:10.1021/j100895a062.

[30] B.M. Venkatesan, R. Bashir, Nanopore sensors for nucleic acid analysis, Nat. Nanotechnol. (2011). doi:10.1038/nnano.2011.129.

[31] D. Branton, D.W. Deamer, A. Marziali, H. Bayley, S.A. Benner, T. Butler, M. Di Ventra, S. Garaj, A. Hibbs, X. Huang, S.B. Jovanovich, S. Lindsay, P.S. Krstic, X.S. Ling, C.H. Mastrangelo, A. Meller, J.S. Oliver, J.M. Ramsey, R. Riehn, M. Wiggin, J.A. Schloss, V. Tabard-Cossa, G. V. Soni, M. Wanunu, The potential and challenges of nanopore sequencing, in: Nanosci. Technol. A Collect. Rev. from Nat. Journals, 2009. doi:10.1142/9789814287005_0027.

[32] Y. Liu, D. Ganser, A. Schneider, R. Liu, P. Grodzinski, N. Kroutchinina, Microfabricated polycarbonate CE devices for DNA analysis, Anal. Chem. (2001). doi:10.1021/ac010343v.

[33] N.M. Toriello, C.N. Liu, R.A. Mathies, Multichannel reverse transcription-polymerase chain reaction microdevice for rapid gene expression and biomarker analysis, Anal. Chem. (2006). doi:10.1021/ac061058k.

[34] P.C.H. Li, Microfluidic Lab-on-a-Chip for Chemical and Biological Analysis and Discovery, 2005. doi:10.1201/9781420027457.

[35] B. Luan, G. Stolovitzky, G. Martyna, Slowing and controlling the translocation of DNA in a solid-state nanopore, Nanoscale. (2012). doi:10.1039/c1nr11201e.

[36] H. Zhang, Q. Zhao, Z. Tang, S. Liu, Q. Li, Z. Fan, F. Yang, L. You, X. Li, J. Zhang, D. Yu, Slowing down DNA translocation through solid-state nanopores by pressure, Small. (2013). doi:10.1002/smll.201301263.

[37] K. Titov, Y. Ilyin, P. Konosavski, A. Levitski, Electrokinetic spontaneous polarization in porous media: Petrophysics and numerical modelling, J. Hydrol. (2002). doi:10.1016/S0022-1694(02)00151-8.

[38] K. Titov, A. Revil, P. Konosavsky, S. Straface, S. Troisi, Numerical modelling of self-potential signals associated with a pumping test experiment, Geophys. J. Int. (2005). doi:10.1111/j.1365-246X.2005.02676.x.

[39] P. Creux, J. Lachaise, A. Graciaa, J.K. Beattie, A.M. Djerdjev, Strong specific hydroxide ion binding at the pristine oil/water and air/water interfaces, J. Phys. Chem. B. (2009). doi:10.1021/jp906978v.

[40] K.G. Marinova, R.G. Alargova, N.D. Denkov, O.D. Velev, D.N. Petsev, I.B. Ivanov, R.P. Borwankar, Charging of Oil−Water Interfaces Due to Spontaneous Adsorption of Hydroxyl Ions, Langmuir. (1996). doi:10.1021/la950928i.

[41] C. Wang, Y. Song, X. Pan, D. Li, Electrokinetic Motion of an Oil Droplet Attached to a Water-Air Interface from below, J. Phys. Chem. B. (2018). doi:10.1021/acs.jpcb.7b10691.

[42] X.J. Li, Y. Zhou, Microfluidic Devices for Biomedical Applications, 2013. doi:10.1021/acs.chemmater.8b01543.

[43] B. Bruijns, A. van Asten, R. Tiggelaar, H. Gardeniers, Microfluidic devices for forensic DNA analysis: A review, Biosensors. (2016). doi:10.3390/bios6030041.

[44] A.M. Foudeh, T. Fatanat Didar, T. Veres, M. Tabrizian, Microfluidic designs and techniques using lab-on-a-chip devices for pathogen detection for point-of-care diagnostics, Lab Chip. (2012). doi:10.1039/c2lc40630f.

[45] D. Wu, J. Qin, B. Lin, Electrophoretic separations on microfluidic chips, J. Chromatogr. A. (2008). doi:10.1016/j.chroma.2007.11.119.

[46] E. Guihen, Recent advances in miniaturization-The role of microchip electrophoresis in clinical analysis, Electrophoresis. (2014). doi:10.1002/elps.201300359.

[47] W. Horwitz, The theory of electrokinetic phenomena, J. Chem. Educ. (1939). doi:10.1021/ed016p519.

[48] D. Li, Single-Phase Electrokinetic Flow in Microchannels, in: Heat Transf. Fluid Flow Minichannels Microchannels, 2013. doi:10.1016/B978-0-08-098346-2.00004-1.

[49] D. Mampallil, D. van den Ende, Electroosmotic shear flow in microchannels, J. Colloid Interface Sci. (2013). doi:10.1016/j.jcis.2012.08.030.

[50] S. Devasenathipathy, J.G. Santiago, K. Takehara, Particle tracking techniques for electrokinetic microchannel flows, Anal. Chem. (2002). doi:10.1021/ac011243s.

[51] D. Ross, T.J. Johnson, L.E. Locascio, Imaging of electroosmotic flow in plastic microchannels, Anal. Chem. (2001). doi:10.1021/ac001509f.

[52] Z. Ding, Y. Jian, W. Tan, Electrokinetic energy conversion of two-layer fluids through nanofluidic channels, J. Fluid Mech. 863 (2019) 1062–1090. doi:10.1017/jfm.2019.6.

[53] R.J. Hunter, Zeta Potential in Colloid Science, 1981. doi:10.1016/B978-0-12-361961-7.50019-5.

[54] H. Daiguji, Ion transport in nanofluidic channels, Chem. Soc. Rev. (2010). doi:10.1039/b820556f.

[55] H. Daiguji, P. Yang, A. Majumdar, Ion Transport in Nanofluidic Circuits, Nano Lett. (2004). doi:10.1021/nl0348185.

[56] M. Malekidelarestaqi, A. Mansouri, S.F. Chini, Electrokinetic energy conversion in a finite length superhydrophobic microchannel, Chem. Phys. Lett. (2018). doi:10.1016/j.cplett.2018.05.007.

[57] C.C. Chang, R.J. Yang, Computational analysis of electrokinetically driven flow mixing in microchannels with patterned blocks, J. Micromechanics Microengineering. (2004). doi:10.1088/0960-1317/14/4/016.

[58] M. Sadeghi, A. Sadeghi, M.H. Saidi, Electroosmotic Flow in Hydrophobic Microchannels of General Cross Section, J. Fluids Eng. (2015). doi:10.1115/1.4031430.

[59] A. Mansouri, A. Vali, L.W. Kostiuk, Electrokinetic power generation of non-Newtonian fluids in a finite length microchannel, Microfluid. Nanofluidics. (2016). doi:10.1007/s10404-016-1735-0.

[60] COMSOL, Introduction to COMSOL Multiphysics 5.3, Manual. (2014). doi:10.1108/JCRE-12-2012-0031.

[61] J. Yang, D.Y. Kwok, Effect of liquid slip in electrokinetic parallel-plate microchannel flow, J. Colloid Interface Sci. (2003). doi:10.1016/S0021-9797(02)00158-3.

[62] S. Il Kim, S.J. Kim, Analysis of the electroviscous effects on pressure-driven flow in nanochannels using effective ionic concentrations, Microfluid. Nanofluidics. (2018). doi:10.1007/s10404-017-2029-x.

[63] G. Karniadakis, A. Beskok, N. Aluru, Microflows and Nanoflows: Fundamentals and Simulation (Interdisciplinary Applied Mathematics), 2005.

[64] K.A. Heyries, M.G. Loughran, D. Hoffmann, A. Homsy, L.J. Blum, C.A. Marquette, Microfluidic biochip for chemiluminescent detection of allergen-specific antibodies, Biosens. Bioelectron. (2008). doi:10.1016/j.bios.2008.02.025.

[65] S. Kim, L. Chen, S. Lee, G.H. Seong, J. Choo, E.K. Lee, C.H. Oh, S. Lee, Rapid DNA hybridization analysis using a PDMS microfluidic sensor and a molecular beacon, Anal. Sci. (2007). doi:10.2116/analsci.23.401.

[66] P.C. Simpson, D. Roach, A.T. Woolley, T. Thorsen, R. Johnston, G.F. Sensabaugh, R.A. Mathies, High-throughput genetic analysis using microfabricated 96-sample capillary array electrophoresis microplates, Proc. Natl. Acad. Sci. U. S. A. (1998). doi:10.1073/pnas.95.5.2256.

[67] M. Hadigol, R. Nosrati, M. Raisee, Numerical analysis of mixed electroosmotic/pressure driven flow of power-law fluids in microchannels and micropumps, Colloids Surfaces A Physicochem. Eng. Asp. (2011). doi:10.1016/j.colsurfa.2010.10.045.

[68] T. Hiemstra, W.H. Van Riemsdijk, A surface structural approach to ion adsorption: The charge distribution (CD) model, J. Colloid Interface Sci. (1996). doi:10.1006/jcis.1996.0242.

[69] Z. Chai, B. Shi, Simulation of electro-osmotic flow in microchannel with lattice Boltzmann method, Phys. Lett. Sect. A Gen. At. Solid State Phys. (2007). doi:10.1016/j.physleta.2006.12.006.

[70] P.J. Kemery, J.K. Steehler, P.W. Bohn, Electric field mediated transport in nanometer diameter channels, Langmuir. (1998). doi:10.1021/la980147s.

[71] A. Mansouri, A. Tarokh, P. Taheri, Ionic current magnetic fields in a two dimensional nanoslit, Chem. Phys. Lett. (2018). doi:10.1016/j.cplett.2018.08.075.

[72] W.J. Lan, D.A. Holden, J. Liu, H.S. White, Pressure-driven nanoparticle transport across glass membranes containing a conical-shaped nanopore, J. Phys. Chem. C. (2011). doi:10.1021/jp204839j.

[73] D.P. Hoogerheide, B. Lu, J.A. Golovchenko, Pressure-voltage trap for DNA near a solid-state nanopore, ACS Nano. (2014). doi:10.1021/nn5025829.

[74] W. Sparreboom, A. Van Den Berg, J.C.T. Eijkel, Transport in nanofluidic systems: A review of theory and applications, New J. Phys. (2010). doi:10.1088/1367-2630/12/1/015004.

[75] S. Pennathur, J.G. Santiago, Electrokinetic transport in nanochannels. 1. Theory, Anal. Chem. (2005). doi:10.1021/ac050835y.

[76] W. Sparreboom, A. Van Den Berg, J.C.T. Eijkel, Principles and applications of nanofluidic transport, Nat. Nanotechnol. (2009). doi:10.1038/nnano.2009.332.

[77] T. Uchiyama, K. Mohri, S. Nakayama, Measurement of spontaneous oscillatory magnetic field of guinea-pig smooth muscle preparation using pico-tesla resolution amorphous wire

magneto-impedance sensor, in: IEEE Trans. Magn., 2011. doi:10.1109/TMAG.2011.2148165.

[78] N. Haned, M. Missous, Nano-tesla magnetic field magnetometry using an InGaAs-AlGaAs-GaAs 2DEG Hall sensor, Sensors Actuators, A Phys. (2003). doi:10.1016/S0924-4247(02)00386-2.

[79] J. Zhai, Z. Xing, S. Dong, J. Li, D. Viehland, Detection of pico-Tesla magnetic fields using magneto-electric sensors at room temperature, Appl. Phys. Lett. (2006). doi:10.1063/1.2172706.

Appendix

The following figures show the results for the electric potential, velocity and magnetic field distributions for both the 3D and 2D models developed for electroosmotic flows:

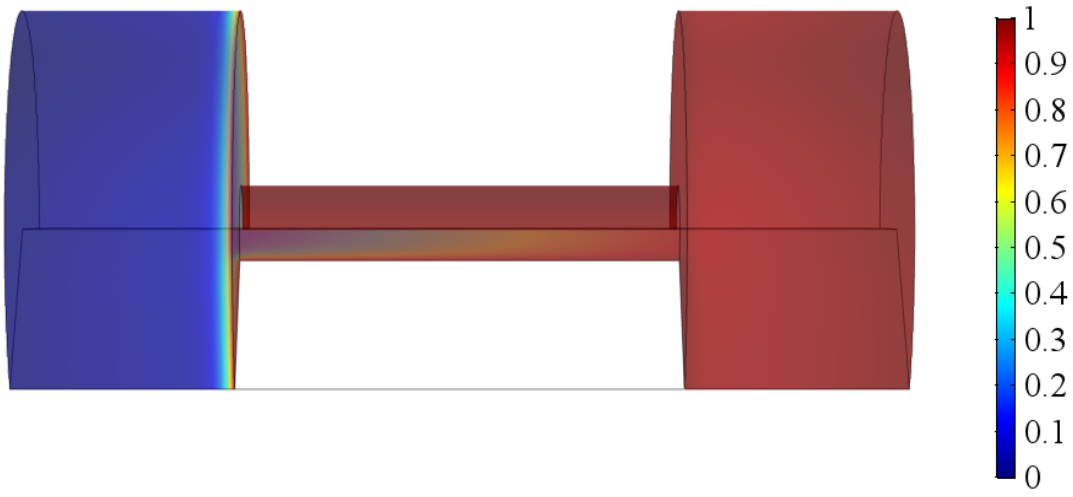

Figure 0.1 3D plot of the steadt state electric potential distribution for electrosomotic flow inside a capillary where each end of the reservoirs has an electrode that creates an electric field. $\kappa a = 5\ \psi_s = 1$.

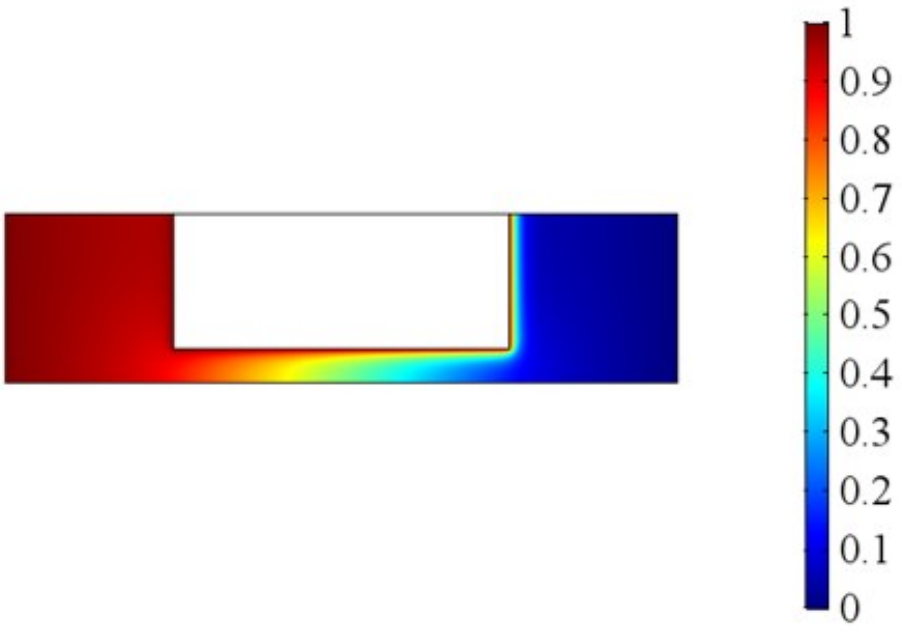

Figure 0.2 2D plot of the steady state electric potential distribution for electrosomotic flow inside a capillary where each end of the reservoirs has an electrode that creates an electric field. $\kappa a = 5\ \psi_s = 1$.

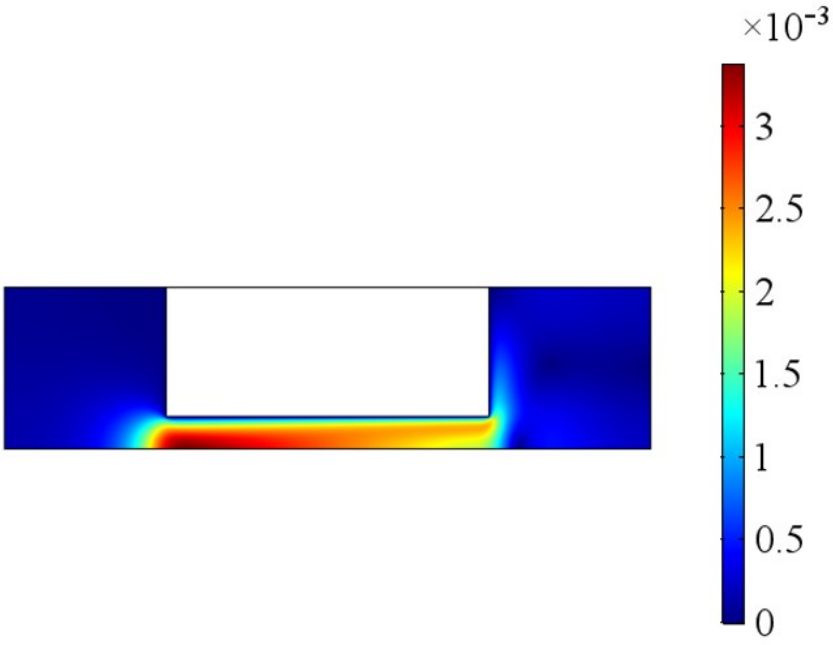

Figure 0.3 2D plot of the steady state velocity distribution for electrosomotic flow inside a capillary where each end of the reservoirs has an electrode that creates an electric field. $\kappa a = 5$ $\psi_s = 1$.

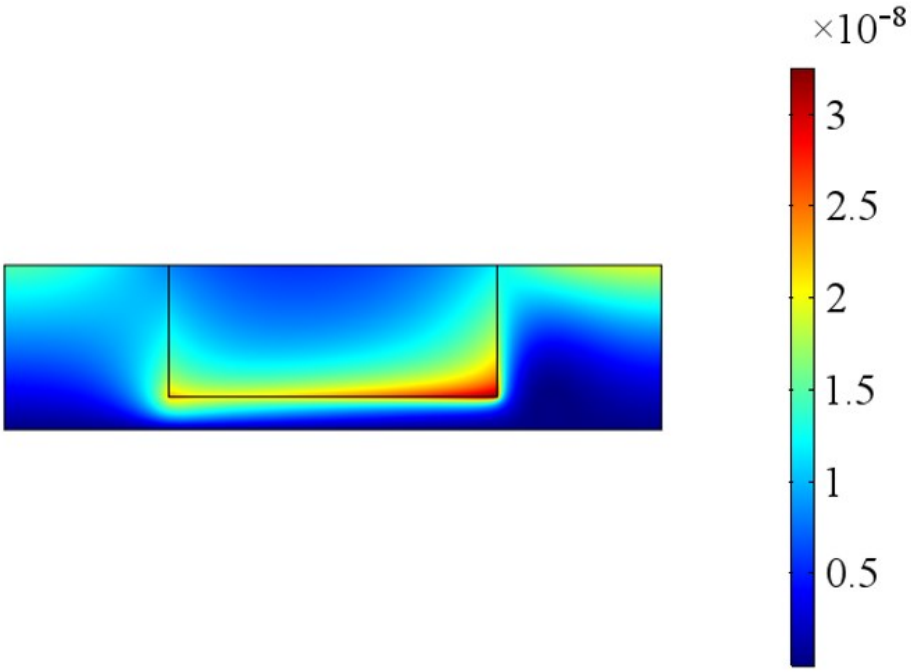

Figure 0.4 2D plot of the steady state magnetic flux density distribution for electrosomotic flow inside a capillary where each end of the reservoirs has an electrode that creates an electric field. $\kappa a = 5\ \psi_s = 1$.

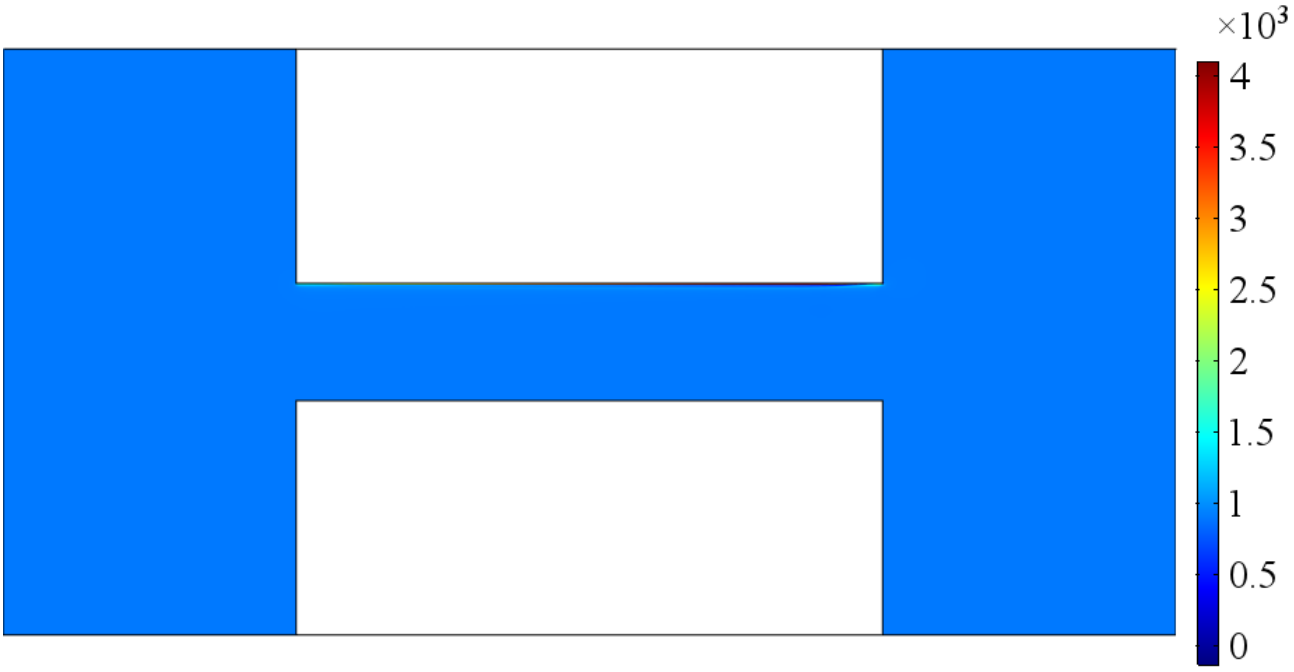

Figure 0.5 2D plot of the steady state pressure distribution for streaming potentail flows inside a slit microchannael. $\kappa H = 10$ $\psi_s = 1$.

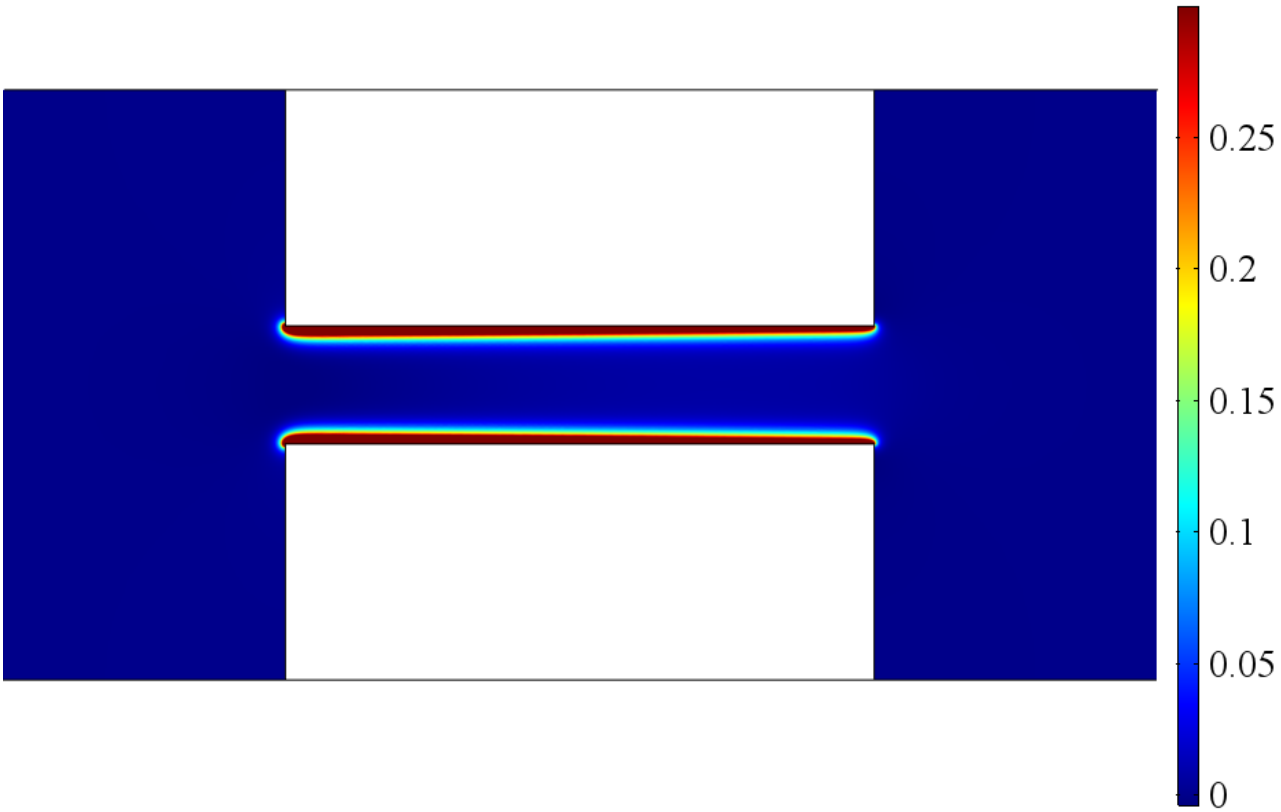

Figure 0.6 2D plot of the steady state pressure distribution for electroosmotic flows inside a capillary where each end of the reservoirs has an electrode that creates an electric field. $\kappa a = 5$ $\psi_s = 1$.

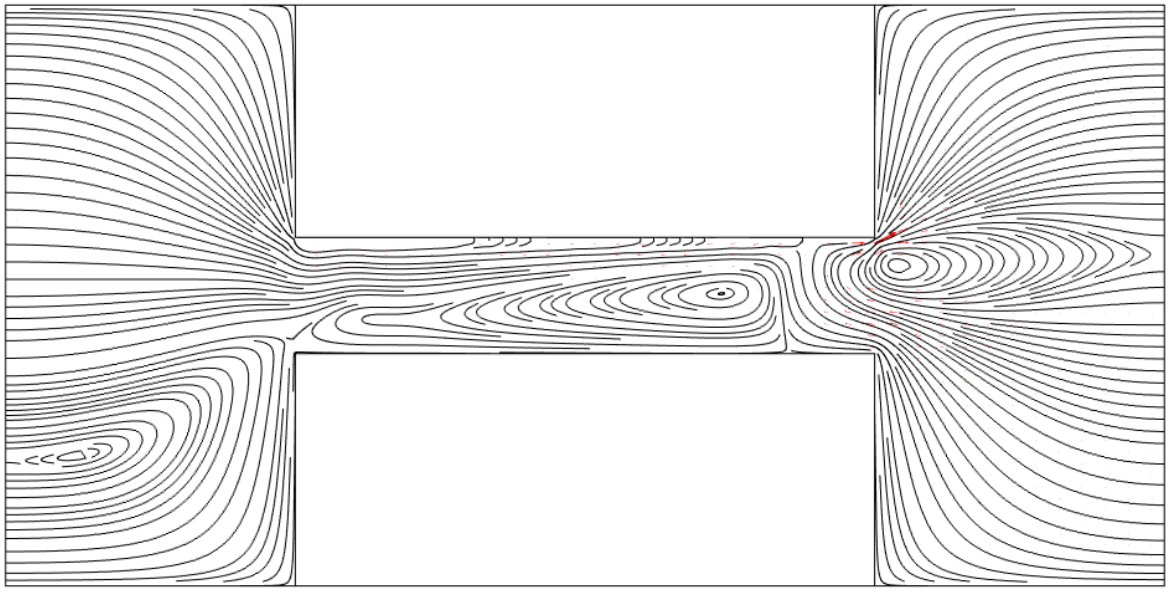

Figure 0.7 2D plot of the recirculation streamlines for streaming potential flows inside a slit microchannel where flow reversal takes place. $\kappa H = 10$ $\psi_s = 7$.